electrochem

MDPI

Article

Molybdenum-Suboxide Thin Films as Anode Layers in Planar Lithium Microbatteries

Ambadi Lakshmi-Narayana [1], Obili M. Hussain [1], Chintalapalle V. Ramana [2], Marco Camacho-Lopez [3], Ashraf Abdel-Ghany [4], Ahmed Hashem [4], Alain Mauger [5] and Christian M. Julien [5,*]

1 Thin films Laboratory, Department of Physics, Sri Venkateswara University, Tirupati 517502, India; narayanalakshmi111@yahoo.com (A.L.-N.); hussainsvu@gmail.com (O.M.H.)
2 Department of Mechanical Engineering, University of Texas at El Paso, El Paso, TX 79968, USA; rvchintalapalle@utep.edu
3 Laboratorio de Investigaci_on y Desarrollo de Materiales Avanzados, Facultad de Química, Universidad Autonoma del Estado de Mexico, Toluca 50925, Mexico; mramanmarco@gmail.com
4 Inorganic Chemistry Department, National Research Centre, 33 El Bohouth Str. (former El Tahir Str.), Dokki-Giza 12622, Egypt; achraf_28@yahoo.com (A.A.-G.); ahmedh242@yahoo.com (A.H.)
5 Institut de Minéralogie, de Physique des Matériaux et de Cosmochimie (IMPMC), Sorbonne Université, CNRS-UMR 7590, 4 place Jussieu, 75005 Paris, France; alain.mauger@upmc.fr
* Correspondence: christian.julien@upmc.fr

Received: 11 April 2020; Accepted: 14 May 2020; Published: 18 May 2020

Abstract: In this paper, we investigate the effects of operational conditions on structural, electronic and electrochemical properties on molybdenum suboxides ($MoO_{3-\delta}$) thin films. The films are prepared using pulsed-laser deposition by varying the deposition temperature (T_s), laser fluence (Φ), the partial oxygen pressure (P_{O2}) and annealing temperature (T_a). We find that three classes of samples are obtained with different degrees of stoichiometric deviation without post-treatment: (i) amorphous $MoO_{3-\delta}$ ($\delta < 0.05$) (ii) nearly-stoichiometric samples ($\delta \approx 0$) and (iii) suboxides $MoO_{3-\delta}$ ($\delta > 0.05$). The suboxide films $0.05 \leq \delta \leq 0.25$ deposited on Au/Ti/SiO_2/flexible-Si substrates with appropriate processing conditions show high electrochemical performance as an anode layer for lithium planar microbatteries. In the realm of simple synthesis, the $MoO_{3-\delta}$ film deposited at 450 °C under oxygen pressure of 13 Pa is a mixture of α-MoO_3 and Mo_8O_{23} phases (15:85). The electrochemical test of the 0.15MoO_3-0.85Mo_8O_{23} film shows a specific capacity of 484 μAh cm^{-2} μm^{-1} after 100 cycles of charge-discharge at a constant current of 0.5 A cm^{-2} in the potential range 3.0–0.05 V.

Keywords: molybdenum suboxides; thin films; pulsed-laser deposition; anodes; lithium microbatteries

1. Introduction

Thin-film technology opens the way for the development of micro-electrochemical power sources powering miniaturized devices such as credit cards, chip units, medical implants and devices, stand-alone sensors, etc. It is also useful for understanding the intrinsic properties of the active materials of lithium batteries (cathode, solid electrolyte, and anode) free of carbonaceous additive and polymeric binder [1]. Thin film electrodes have the advantage of shortening the ionic and electronic pathways, which enhances high-rate cycle ability.

Molybdenum oxides (MoO_3 and its $MoO_{3-\delta}$ suboxides with stoichiometric deviation $\delta < 1$) belong to the class of materials that offer a tunability of their intrinsic electronic properties from wide bandgap semiconductor MoO_3 to metallic MoO_2 [2]. The varieties of oxidation states from Mo^{6+} to Mo^{4+} in $MoO_{3-\delta}$ films makes them highly attractive in the field of energy storage and conversion and they have found application in all-solid state thin film microbatteries (TFμBs) [3,4], electrochemical

supercapacitors [5], gas sensors [6], electrochromic devices [7], solar cells [8,9], anode interlayers for photovoltaic devices [10], smart windows [11], light-emitting diodes [12], etc. These devices take advantage of the changes in the degree of crystallinity, cationic environment, stoichiometry deviation, band gap energy and electronic conductivity, which can be controlled by the growth conditions.

Regarding their electronic structure, the molybdenum oxide phases can be classified in four groups: (i) the strictly stoichiometric MoO_3 (layered structure, orthorhombic, *Pnma* symmetry) is insulator, (ii) the nearly-stoichiometric $MoO_{3-\delta}$ (with $\delta < 0.03$), which retains the orthorhombic symmetry, is unintentionally an *n*-type semiconductor at ambient conditions, partly due to intrinsic point defects related to oxygen vacancies (V_O) and molybdenum interstitials (Mo_i) [13], (iii) the defective $MoO_{3-\delta}$ (with $0.03 < \delta < 0.11$) and (iv) Mo_nO_{3n-1} suboxides (Magnéli phases, n = 4–9), which collapse into ReO_3-type structures with crystallographic shear planes due to the destabilization of the MoO_3 structure by the loss of oxygen [14–19]. The schematic representation of the crystal structure of the layered α-MoO_3 phase and the vacancies of the three inequivalent oxygen positions O1 (apical), O2 (corner-sharing) and O3 (edge-sharing) are shown in Figure 1 [20]. An O1 vacancy ($V_{O(1)}$) leads to two localized electrons on the neighboring Mo that are thus in the Mo^{4+} ($4d^2 5s^0$) configuration; O2 and O3 vacancies create a bipolaron with electrons localized on two separate Mo^{5+} sites in the first and second coordination spheres for $V_{O(2)}$ and on the opposite side of the vacancy for $V_{O(3)}$ [21]. At higher vacancy concentration, the shear structure is energetically more favorable than the point defects [22]. The known Mo suboxides include Mo_4O_{11}, Mo_5O_{14}, Mo_6O_{17}, Mo_8O_{23}, Mo_9O_{26} ($Mo_{18}O_{52}$) and $Mo_{17}O_{47}$, which are formed by a mixture of Mo oxidation states between +6 and +4.

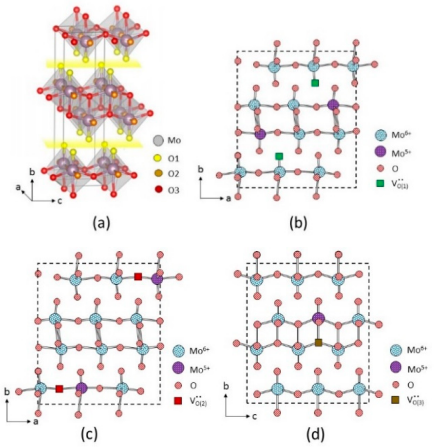

Figure 1. Crystal structure of the layered α-MoO_3 phase (**a**) and the vacancies of the three inequivalent oxygen positions O1 (apical) (**b**), O2 (corner-sharing) (**c**) and O3 (edge-sharing) (**d**). Adapted from [20]. Copyright 2016 American Chemical Society.

Figure 2 shows a schematic diagram of the electronic states of molybdenum oxides as a function of the oxygen vacancies. The electronic character varies from insulator (MoO_3) to semiconductor ($MoO_{3-\delta}$) and finally to metal-like (Mo_9O_{26}), in agreement with conductivity measurements [21]. The electron distribution in pure MoO_3 follows the ionic model (Mo^{6+} and O^{2-}) corresponding to the Mo $4d^0$ configuration. For non- stoichiometric MoO_3 oxides, extended Mo 4*d* states, which then lie in the bandgap as gap states due to the occurrence of Mo^{5+} and Mo^{4+} ions, are filled by electrons donated from oxygen vacancies. The formation of oxygen deficiency (termed also as sub-stoichiometric) not only produces an increase of the electrical conductivity σ_e [23] owing to the additional gap states, but also increases the surface energy of the particles and promotes electrochemical reactions [21,24]. Magnetic susceptibility measurements showed that MoO_3, MoO_2 and Mo_nO_{3n-1} shear suboxides in between are all feebly paramagnetic.

The $MoO_{3-\delta}$ suboxide phases (with $0 < \delta < 0.25$) exhibit Li-insertion capacity much higher than that of stoichiometric MoO_3 phase, which justifies the efforts to fabricate them under the form of thin films.

For the development of these technologies, oxygen vacancies are easily generated in the $MoO_{3-\delta}$ materials prepared in a thin film architecture by optimizing the deposition conditions [25]. Like stoichiometric MoO_3, sub-stoichiometric $MoO_{3-\delta}$ thin films can be obtained by evaporation in a vacuum at relatively low temperature (T < 500 °C) or in reducing atmosphere. However, few works explore the effect of oxygen deficiency and electrical conduction enhancement on energy storage properties [26,27].

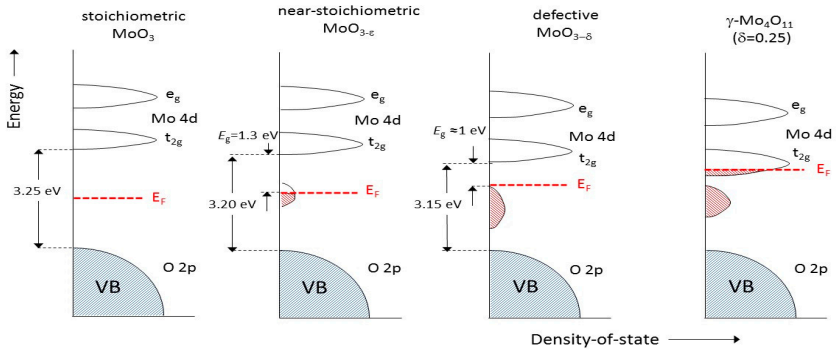

Figure 2. Schematic diagram of the electronic states of molybdenum oxides as a function of the oxygen vacancies. The electronic character varies from insulator (MoO_3, $\sigma_e > 10^{-9}$ S cm^{-1}) to semiconductor (defective Mo_9O_{26}, $\sigma_e \approx 10^{-2}$ S cm^{-1}) to metal-like (γ-Mo_4O_{11}, $\sigma_e \approx 10^{4}$ S cm^{-1}).

$MoO_{3-\delta}$ thin films have been easily prepared using a broad variety of physical vapor deposition (PVD) methods, including thermal evaporation [28,29], flash evaporation [30], electrodeposition [31], d.c. and r.f. magnetron sputtering [3,32–34], spay-pyrolysis [35], electron-beam evaporation [36,37], dip-coating [9], spin-coating [38], atomic layer deposition (ALD) [39], pulsed layer deposition (PLD) [4,40–51] and chemical vapor deposition (CVD) [52,53]. However, few works report the spin-coating deposition of $MoO_{3-\delta}$ via a low-temperature solution process [54].

It is well known that PLD, based on the process of the transportation of material (laser ablation), is a powerful technique to fabricate multicomponent oxide dense films with high purity. Generally, the stoichiometry can be easily tuned by a control of growth rate (R_g), laser fluence (Φ), substrate temperature (T_s), oxygen partial pressure (P_{O_2}) and morphology of the substrate [55]. Two strategies are used to fabricate well-crystallized $MoO_{3-\delta}$ thin films: (i) the deposition is carried out in an O_2 atmosphere and at elevated T_s, which provides Mo oxidation inside the chamber during the growth process [53], (ii) the film oxidation is prepared in a vacuum with post-annealing at a moderate temperature (T_a) without the use of reactive O_2 and substrate heating [50,51]. In view of the numerous studies of $MoO_{3-\delta}$ thin films prepared using the PLD technique, it is important to compare the structural properties of films obtained under different experimental conditions [56]. Hussain et al. optimized the deposition conditions (T_s = 200 °C, P_{O2} = 13 Pa) for crystalline α–MoO_3, while at an oxygen partial pressure less than 13, Pa sub-stoichiometric films with α–β mixed phases were found [43]. Camacho-Lopez investigated the structural transition in PLD films; the as-deposited $MoO_{1.99}$ is oxidized to $MoO_{2.77}$ by heat treatment at 200 °C for 14 h in air [43]. Torres et al. [46] studied MoO_3 films fabricated using a thermal laser deposition method with a CO_2 laser (λ = 10.6 μm) at an intensity of 0.73 W mm^{-2} under oxygen pressure of 0.5 Pa. For a substrate temperature $T_s \geq 350$ °C, the XRD patterns displayed both (0k0) and (0kl) orientations representing α-β mixed MoO_3 phases. Robinson-Azariah et al. studied the effect of the repetition rate (R_{rl}) on the composition of MoO_x PLD films deposited at a fluence of 150 mJ cm^{-2} on fluorine-doped tin-oxide-coated glass substrate kept at 25 °C under O_2 gas at a pressure of 5 Pa [49]. While XRD patterns exhibited the orthorhombic α-MoO_3 phase for all films, the XPS studies showed the presence of Mo^{5+} oxidation state giving oxygen-deficient films $MoO_{2.98}$ and $MoO_{2.75}$ at R_{rl} of 2 and 10 Hz, respectively. PLD $MoO_{3-\delta}$ suboxide films (~100 nm thick) with different compositions were deposited on fused silica slides using two excimer laser sources, XeF (λ_{ex} = 351 nm, Φ = 85 mJ) and KrF (λ_{ex} = 248 nm, Φ = 200 mJ), without introduction of oxygen in the chamber and subjected to post-annealing at a temperature, T_a, in the

range of 300–500 °C for 4 h in air [50]. The as-prepared films were amorphous (dark color) and started to be partially crystallized at $T_a \approx 400$ °C; the chemical surface state studied using XPS exhibited an O/Mo ratio of 2.95, which decreased to 2.78 upon heating at 500 °C. Subsequent annealing at 300 °C in vacuum reduced the deviation from stoichiometry to $MoO_{2.65}$ [57].

In this work, we investigate the growth of molybdenum-oxide thin films (oxygen deficient $MoO_{3-\delta}$ and Mo_nO_{3n-1} suboxides) deposited on Au/Ti/SiO_2/flexible-Si substrates using a PLD technique with appropriate processing conditions. Relationships are established between structure, texture, cationic environment and deposition conditions such as substate temperature, ablation power and oxygen partial pressure. The electrochemical performance of as-prepared and heat-treated films are examined as anode in TFμBs. Tuning the oxygen vacancies in $MoO_{3-\delta}$ suboxide thin films appears to be one of the best engineering strategies to obtain an extended cycling stability and a decrease of the overpotential. The introduction of oxygen vacancies accelerates the electron transport, which can play a positive role in boosting the Li^+ diffusivity. To the best of our knowledge, this is the first report on the correlation between the nanoscale structure of $MoO_{3-\delta}$ thin films and their electrochemical properties. The reversible lithium insertion/deinsertion reaction at ambient temperature makes them a candidate for a negative electrode in lithium microbatteries.

This paper is organized as follows. Section 2 presents the experimental techniques (substrate preparation, growth and characterization). In Section 3, detailed results describe the fundamental properties of films including structure, morphology and composition. The next section, Section 4, reports the electrochemical properties of $MoO_{3-\delta}$ thin films (charge-discharge profiles and Li^+ ions kinetics). Finally, a general discussion is provided in Section 5, comparing the properties of as-prepared PLD $MoO_{3-\delta}$ films with those reported in the literature.

2. Materials and Methods

2.1. Preparation of Au/Ti/SiO_2/flexible-Si Substrates

Au/Ti/SiO_2/Si stacking multilayers were used as substrates, in which the Si chip is the flexible mechanical support (12 μm thick, ULTRATHIN, Virginia Semiconductors Inc., Fredericksburg, VI, USA), the SiO_2 film (100 nm thick) has a unique role of electrical insulation between the current collector (Au/Ti) and Si wafer. The gold film acts as current collector, while the titanium layer enhances the mechanical adhesion to the SiO_2 layer. The multilayered substrates were fabricated according to the following sequence. (i) Silicon chips were treated according the RCA-type cleaning procedure [58]. (ii) The SiO_2 layer (about 100 nm thick) was produced by cleaning the Si chips in H_2SO_4/H_2O_2 solution then rinsed in hydrogen fluoride. (iii) the current collector was formed via metallization with a 20-nm thick Ti layer deposited using radio-frequency (RF) magnetron sputtering then metallized with a 20-nm thick Au film. A scheme representing the stack of the different layers is shown in Figure 3a.

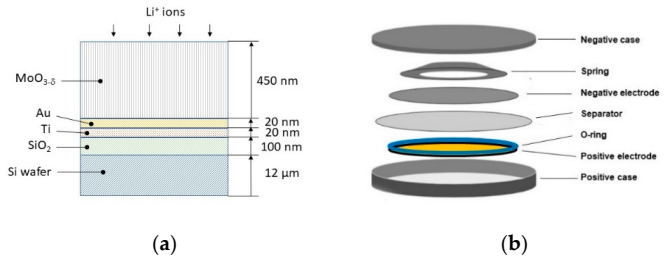

(**a**) (**b**)

Figure 3. Schematic representation of (**a**) the cross-sectional view of the $MoO_{3-\delta}$ thin film electrode deposited on the multilayer substrate and (**b**) the modified CR2477-type coin cell.

2.2. MoO_x Thin Films Fabrication

$MoO_{3-\delta}$ thin films were deposited on the Au/Ti/SiO_2/Si multilayer substrates described above. The target was composed of MoO_3 powders synthesized by solid-state reaction from molybdic acid

(H_2MoO_4) as precursor (Merck KGaA, Darmstadt, Germany, 99.99% grade). The product was ground for 3 h and pressed into a pellet at a pressure of 392 MPa. Subsequently, the pellet was heated at 10 °C min^{-1} and sintered at 650 °C for 3 h in air to yield a target with a density of about 91% of that of dense MoO_3 (4.2 g cm^{-3}). $MoO_{3-\delta}$ thin films were deposited using PLD on substrates maintained in the range $25 \leq T_s \leq 500$ °C. The target was ablated using a KrF excimer laser λ = 248 nm (COMPex 201, Coherent, Göttingen, Germany) with laser fluence of 0.2–1.0 J cm^{-2} and repetition rate of 10 Hz. The target was rotated at 10 rotations min^{-1} to obtain homogenous thin films and circumvent complete depletion of the material at the same spot. The target-to-substrate distance was 4 cm, and the incident laser beam ablated the target surface with an angle of 45°. The system chamber was evacuated to a base pressure of 0.4 mPa prior to film deposition. During reactive deposition, the chamber was filled with pure oxygen gas maintained at P_{O_2} in the range 0.5–13 Pa to obtain $MoO_{3-\delta}$ films with different deviations from stoichiometry. The thickness of the PLD-prepared $MoO_{3-\delta}$ films was ~450 ± 5 nm.

2.3. Film Characterization

The phase and structure of as-prepared $MoO_{3-\delta}$ films was characterized using X-ray diffraction (XRD), Raman scattering (RS) and Fourier transform infrared (FTIR) spectroscopy. XRD patterns were investigated (X-ray diffractometer 3003 TT, Siefert, Leuven, Belgium) using a CuKα radiation source (λ = 0.15406 nm) in the 2θ-range of 10°–70° with a scan speed of 0.03 degree s^{-1}. The vibrational studies were recorded using Raman spectroscopy at a spectral resolution of ≈1 cm^{-1} (Jobin Yvon HR800UV, Longjumeau, France) using an excitation wavelength of 632.8 nm (He:Ne laser) and using Fourier transform infrared (FTIR) spectroscopy (VERTEX 80v, Bruker, Karlsruhe, Germany) in the spectral range 100–1000 cm^{-1}. The optical absorption studies were carried out using a UV−visible spectrophotometer (UV-VIS-NIR, Hitachi U3400, Tokyo, Japan). The chemical valence state of Mo and surface chemical composition were probed using X-ray photoelectron spectroscopy (XPS, K-Alpha-Thermo Scientific spectrometer, Dreieich, Germany) with a monochromatic Al K_α X-ray source (λ = 1486.68 eV). The surface morphological characteristics of the films were studied using scanning electron microscope (SEM, Carl Zeiss, EVO-MA15, Oberkochen, Germany). The surface crystallography was investigated using reflection high-energy electron diffraction (RHEED, EFZ4 device, Carl Zeiss, Germany). The surface topography was analyzed using atomic force microscopy (AFM, Park NX10, Park Sytems, Suwon, Korea). Thickness of the films was measured using an optical profilometer (model Profilm3D, Filmetrics, San Diego, CA, USA).

Investigation of the electrochemical properties of $MoO_{3-\delta}$ thin film (5 cm^2 in area, 450 nm in thickness) was carried out using CR2477-type coin cells (Renata, Brive, France). Particular attention was paid to the coin-cell assembly by addition of an O-ring to avoid the presence of Li with Si and SiO_2 materials (Figure 3b). Non-aqueous Li//$MoO_{3-\delta}$ cells were assembled in argon-filled glovebox with Li foil as a combined counter and reference electrode and Whatman GF/D borosilicate glass fiber as separator. The aprotic electrolyte was 1 mol L^{-1} $LiPF_6$ dissolved in ethylene carbonate and dimethyl carbonate (EC:DMC; 1:1 *w*/*w*). Data were collected using an electrochemical analyzer CHI 608C (CH Instruments Inc., USA) at a current density of 10–200 μA cm^{-2}. For a transfer of 6 moles of electrons per Mo, the current density of 1.17 A g^{-1} corresponds to 1C rate. Electrochemical impedance spectroscopy (EIS) data were collected in the range 0.1 Hz–1 MHz with a bias voltage of 5 mV.

3. Results

3.1. Structural Properties

The structure of PLD $MoO_{3-\delta}$ thin films was investigated using XRD, Raman and FTIR spectroscopy. All the films show uniform thickness, but they vary from dark blue to white in color as a function of the deposition parameters. Figure 4a,b shows the XRD diagrams of PLD $MoO_{3-\delta}$ thin films prepared under different conditions of temperature and oxygen partial pressure. When deposited at T_s = 25 °C, at any P_{O_2} the films are amorphous (a-MoO_3) in nature. Their XRD

spectrum displays a broad band centered at $2\theta = 23°$ characteristic of an amorphous phase. For films deposited at $T_s = 100$ °C, the XRD spectra display the patterns of the mixed phase with both (0*k*0) and (0*kl*) orientations of the α- and β-MoO_3, respectively, the β-MoO_3 phase being characterized by the (011) and (022) reflections (JCPDS card No. 47-1081). For films prepared in the range $150 < T_s < 380$ °C, the XRD reflections are those of the unique α-$MoO_{3-\delta}$ phase indexed to the (0*k*0) plane reflections. They give evidence of a highly preferred orientation, i.e., basal plane parallel to the substrate surface. These lines match well with the standard patterns of the orthorhombic α-MoO_3 phase (JCPDS card No. 05-0508). Moreover, in contrast to the crystalline MoO_3, the broadened diffraction peak located at $2\theta \approx 25°$ is related to the nano-size of the crystallites and the distorted layered structure that is in accordance with published results [59,60]. For the single α-$MoO_{3-\delta}$ phase, the ratio between intensities of the (020) and (060) lines increases with the increase of the substrate temperature. Their intensities are almost identical for $T_s = 350$ °C. Similar trends were observed by Julien et al. at a lower temperature of 250 °C for flash-deposited films [31]. The XRD patterns of the $MoO_{3-\delta}$ films deposited at $T_s > 400$ °C contain two distinct sets of reflections attributed to the coexistence of the α-$MoO_{3-\delta}$ and Mo_8O_{23} phases. This latter phase is well defined with reflections at $2\theta \approx 19.9$, 21.8, 22.4 and 26.1° corresponding, respectively, to the (201), (010), (204) and (302) crystal planes of the monoclinic structure, *P*2/*c* space group (JCPDS Card No. 84-1247). In summary, several remarks are worth making: (i) the deposition temperature and the partial oxygen pressure are the preponderant parameters tuning the film stoichiometry, while the laser fluence governs mainly the deposition rate, (ii) the best crystallinity of the single α-$MoO_{3-\delta}$ phase is obtained for films deposited at moderate temperature, (iii) with the increase of the adatom mobility, the thermodynamics favor the hierarchy α-MoO_3, α-β-$MoO_{3-\delta}$ < α-$MoO_{3-\delta}$ < Mo_8O_{23}, and (iii) an increase in T_s up to 400 °C favors the formation of films with high oxygen deficiency. The change in the oxygen deficiency has also been observed on films fabricated using different techniques. Guerfi et al. reported the growth by electrodeposition of $MoO_{2.8}$ (Mo_5O_{14}) film at room temperature. This metastable tetragonal phase with a strong preferred orientation along the plane (10,10,0) transformed to orthorhombic MoO_3 after heat treatment at 260 °C [61]. This behavior has been investigated for $MoO_{3-\delta}$ films fabricated using reactive RF-magnetron sputtering [62], electron beam evaporation [37], plasma-assisted activated reactive evaporation [63] and CVD [64]. Note that the deviation from stoichiometry can be evidenced by studying the fundamental absorption edge, which can be evaluated in terms of direct inter-band transitions. The optical band-gap depends on oxygen vacancies as donor centers close to the valence band. Julien et al. showed that the optical band-gap of $MoO_{3-\delta}$ films deposited at 25 °C is 3.37 eV (large δ value) and decreases to 2.80 eV for the films prepared at 300 °C (small δ value) [31]. Sivakumar et al. [37] reported a band-gap of 2.8 eV for films deposited on glass substrate maintained at 25 °C (light gray in color), decreasing to 2.35 eV when deposited at 200 °C (deep blue color).

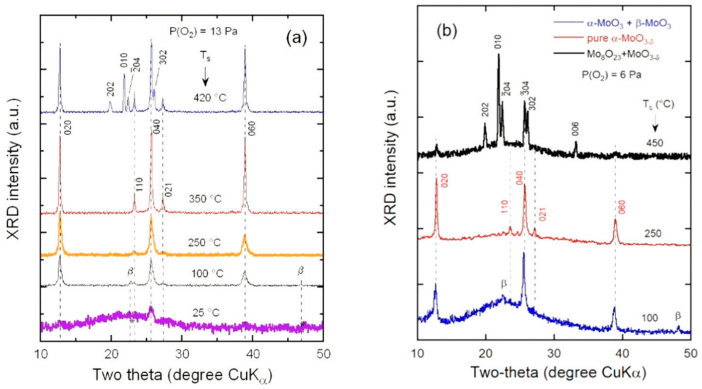

Figure 4. The X-ray diffraction patterns of $MoO_{3-\delta}$ films deposited using the pulsed layer deposition technique under (**a**) $P_{O2} = 13$ Pa and (**b**) $P_{O2} = 6$ Pa. Films were deposited at various substrate temperatures on silicon wafer. Bragg lines have been indexed in the orthorhombic system (*Pbnm* S.G.). (0*kl*) reflections of the β-MoO_3 phase are marked by β.

Vibrational spectroscopies, Raman and FTIR, are powerful probes for the analysis of the short-range order in solids. They are used to confirm the presence of O-defects in $MoO_{3-\delta}$ films [65,66]. Figure 5a displays the Raman scattering spectra of PLD $MoO_{3-\delta}$ thin films deposited at temperature in the range 25–300 °C. Data were collected using the laser excitation wavelength of 632.3 nm. Analysis of spectral features is based on stretching and bending modes of octahedral MoO_6 entities building the MoO_3 framework. In Figure 5a, there are four intense modes in the range of 600–1100 cm^{-1}, which are the characteristic bands inherent to the fully oxygenated α-MoO_3. They are located at 995, 900, 820 and 660 cm^{-1} corresponding to the asymmetrical (A_g, ν_{as} Mo=O) and symmetrical (A_g, ν_s Mo=O) stretching vibrations of the terminal Mo=O double bonds and to the asymmetrical (B_{2g}, B_{3g}, ν_{as} O-Mo–O) stretching vibrations of O–Mo–O bonds, respectively [41,67]. The Raman active modes in the low-frequency region at 283 and 340 cm^{-1} are attributed to the Mo-O-Mo bending vibrations [68]. The deposition temperature-dependent vibrational properties and changes in the chemical bonds were successfully analyzed based on the concept of group frequency developed by Cotton and Wing [69]. The relative intensities of vibration modes and Raman shifts of MoO_x compounds are significantly impacted by the size and shape of crystallites and by the crystal orientation as well [70]. Furthermore, even for a small stoichiometric deviation in $MoO_{3-\delta}$ ($\delta < 0.04$) a frequency shift of the vibrational modes is observed in the Raman spectrum, indicating a weaker Mo-O bonding due to oxygen deficiency [71]. The Raman spectra of $MoO_{3-\delta}$ thin films show clearly the change in morphology and composition from amorphous a-MoO_3 and α-$MoO_{3-\delta}$ to single crystal α-MoO_3. These structural modifications are visualized by a shift of the three high-frequency stretching modes at 995, 820, and 660 cm^{-1} for orthorhombic α-MoO_3 to 976, 800 and 648 cm^{-1} for oxygen-deficient $MoO_{3-\delta}$. The presence of Mo^{5+} defects can be identified by the appearance of new Raman bands compared with the spectrum of stoichiometric MoO_3. The Raman peaks located at 771 cm^{-1} confirm the presence of a localized Mo^{5+} intermediate oxidation state produced by oxygen vacancies in α-$MoO_{3-\delta}$. The same set of peaks is observed in the Raman spectrum of Mn_4O_{11} ($MnO_{2.75}$), in which the average oxidation state of Mo is +5.5. Chen et al. [72] investigated the presence of oxygen vacancies in MoO_3 nanobelts (20 nm thick) using Raman spectroscopy, which was evidenced by the redshift of the main Raman peaks. Moreover, Lee et al. have assigned the peak at 400 cm^{-1} to vibrational bonds between Mo^{5+} and oxygen [73]. The Raman spectrum of films deposited at 450 °C presents the superposition of the α-MoO_3 and Mo_8O_{23} vibrational modes. The peaks at 225, 255, 377, 675, 902 and 958 cm^{-1} are assigned to the *m*-Mo_8O_{23} phase [62,74].

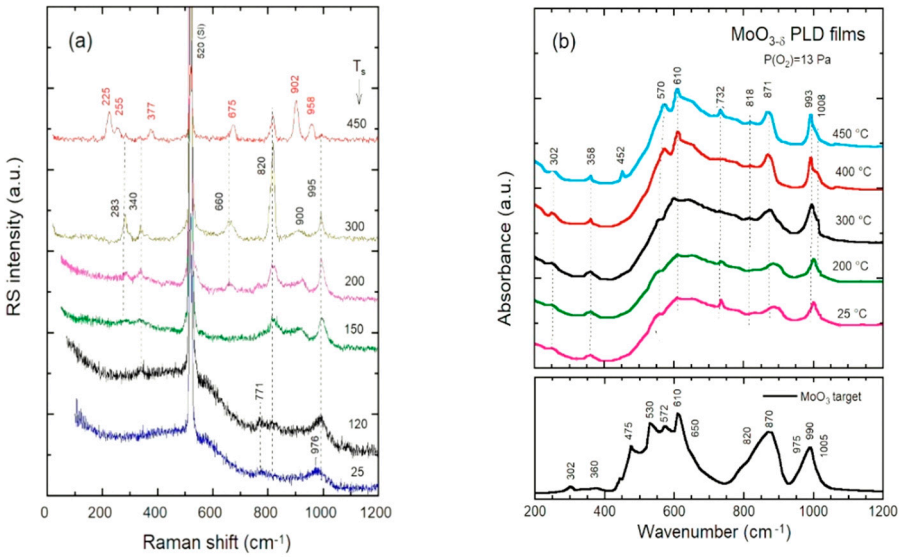

Figure 5. Vibrational spectra of PLD $MoO_{3-\delta}$ thin films deposited at various temperatures. Each spectrum is shifted vertically for clarity. (**a**) Raman scattering spectra collected with the laser excitation wavelength of 632.3 nm. Frequencies marked in red are those of Mo_8O_{23}. (**b**) FTIR spectra of $MoO_{3-\delta}$ thin films and MoO_3 target (bottom).

The FTIR absorbance spectra of PLD $MoO_{3-\delta}$ thin films grown at various temperatures ($25 \leq T_s \leq 400$ °C) are presented in Figure 5b. In the high-wavenumber region (500–1000 cm^{-1}), the broad absorption band is resolved into several sub-bands at 570, 610, 818, 871, 993 and 1008 cm^{-1} corresponding to the stretching modes involving (O-Mo_2), (O-Mo_3) and (Mo=O) bonds. The broader peak at ~650 cm^{-1} is attributed to bridging Mo-O-Mo bonds of Mo^{6+} [75,76]. The splitting of the Mo=O stretching at 993 and 1008 cm^{-1} reflects the good crystallinity of the films. It corresponds to the vibration of the zig-zag rows, which is a typical feature of the layered α-MoO_3 phase. The bending infrared modes are observed in the low-frequency region (200–500 cm^{-1}). The presence of Mo^{5+} defects can be identified by the appearance of new IR bands at 732 cm^{-1} compared with the spectrum of stoichiometric MoO_3. This mode is assigned to the stretching mode of Mo^{5+}. Dun et al. observed the mode characteristic of the bridging O-Mo_2 of Mo^{5+} at 700 cm^{-1} [77]. Similarly to the Raman patterns, the FTIR spectra of sub-stoichiometric $MoO_{3-\delta}$ films display a frequency shift upon oxygen deficiency. This is consistent with the literature reports. Sun et al. reported the ν(O-Mo_2) band shifts towards lower wave numbers (868 → 721 → 683 cm^{-1}) for sub-stoichiometric α-$MoO_{3-\delta}$ due to the reduction of the MoO_3 lattice through the formation of oxygen vacancies in the doubly coordinated oxygen. In contrast, the ν(O=Mo) band shifts towards higher wavenumbers (948 → 973 → 975 cm^{-1}) [78].

3.2. Composition

The composition of as-deposited $MoO_{3-\delta}$ thin films was characterized by high-resolution XPS. Figure 6a–c shows the XPS spectra of the Mo 3*d* core level in $MoO_{3-\delta}$ thin films deposited on substrate maintained at 25, 300 and 450 °C under oxygen pressure of 6 Pa. The XPS spectra were analyzed by evaluating the peak area of elements using Gaussian profiles after removing the secondary electron background. All XPS spectra can be deconvoluted using two Mo 3*d* doublets ($3d_{5/2}$ and $3d_{3/2}$). The first doublet centered at 236 and 232.8 eV is typical of the Mo^{6+} state with a spin-orbit separation of ~3.2 eV, whereas the second one located at 234.6 and 231.9 eV is due to Mo^{5+} [79,80]. The film deposited at 25 °C is highly disordered and shows a large stoichiometric deviation (Figure 6a). When deposited at 300 °C, the XPS spectrum is dominated by the Mo^{6+} doublet that corresponds to nearly MoO_3 films (Figure 6b), while the increase of the Mo^{5+} doublet is observed for films prepared at $T > 400$ °C (Figure 6c). In the case of film deposited at 450 °C, the combination of XRD and XPS data provides the composition $0.85Mo_8O_{23}$-$0.15MoO_3$. From the variation of the O/Mo ratio (Figure 6), we can distinguish three regions related with the morphology and composition of the films, i.e., in region (I) the $MoO_{3-\delta}$ films are highly disordered and off-stoichiometric, region (II) includes near-stoichiometric films, and region (III) encompasses oxygen deficient lattices. These results show that Mo cation exists in the highest oxidation state in $MoO_{3-\delta}$ thin films grown in the range $200 \leq T_s \leq 400$ °C, which suggests an efficient gas phase reaction in the plume of the laser ablation. When the temperature increases beyond 400 °C, the films contain Mo in lower oxidation state $+6 < n < +5$ due to dissociation. The re-evaporation from the film surface making the incorporation of oxygen into the lattice more difficult cannot be ruled out.

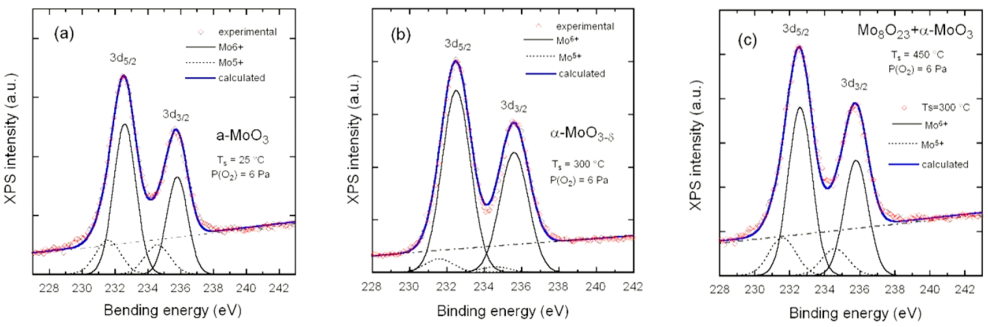

Figure 6. XPS patterns of $MoO_{3-\delta}$ films grown using the PLD technique under $P_{O2} = 6$ Pa. (**a**) Amorphous $MoO_{3-\delta}$ deposited at 25 °C, (**b**) crystalized $MoO_{3-\delta}$ deposited at 300 °C and (**c**) Mo_8O_{23}+$MoO_{3-\delta}$ deposited at 425 °C.

Taking k as the ratio of the quantity of Mo^{5+}/Mo^{6+} calculated from the ratio of the integrated peak area, the stoichiometric deviation can be calculated by the relation [81]:

$$\delta = 3 - \frac{1}{2}\left[5 + (k+1)^{-1}\right] \quad (1)$$

Table 1 reports the composition of $MoO_{3-\delta}$ thin films as a function of the deposition temperature calculated using Equation (1) from data in Figure 7. It is well known that the α-MoO_3 phase retains the orthorhombic structure until the O/Mo ratio is reduced to about 2.89 with the formation of the shear phase like Mo_9O_{26} or Mo_8O_{23} (monoclinic, $P2/c$ space group) for higher concentrations of oxygen vacancies. However, it is unlikely that oxygen vacancies remain as point defects, as ordering of oxygen vacancies has been observed at very low concentrations [82].

Table 1. Composition of the PLD $MoO_{3-\delta}$ thin films evaluated from the analysis of XPS spectra.

T_s (°C)	k	δ	Composition
25	0.55	0.178	a-$MoO_{2.822}$
300	0.04	0.018	α-$MoO_{2.982}$
450	0.27	0.106	0.85Mo_8O_{23}-0.15MoO_3

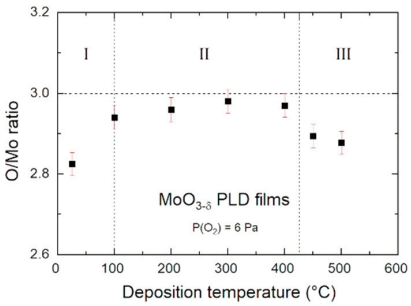

Figure 7. Variation of the O/Mo ratio as a function of the deposition temperature.

This finding is consistent with previous investigations [45,83,84]. For all films, the minor 3*d* doublet for Mo^{5+} in the XPS spectra indicates that the perfectly stoichiometric MoO_3 was not reached. These results suggest that the growth of $MoO_{3-\delta}$ thin films with tunable oxygen vacancies favors their electrical properties as anode materials for electrochemical micro-systems. The $MoO_{3-\delta}$ films thermally deposited at 25 °C are sub-stoichiometric with an O/Mo atomic ratio of 2.73 increasing to 2.91 after annealing at 200 °C, while heat treatment at 400 °C reduces the oxygen vacancy defects [83]. Fernandes-Cauduro et al. investigated the effects of in situ annealing in $MoO_{3-\delta}$ thin films prepared using reactive sputtering. The deviation from stoichiometry decreases from 0.125 to 0.11 for film treated at 200 °C but it then increases (δ = 0.20) for the film formed at 500 °C, which is explained by the appearance of the 6% Mo^{4+} state at the surface [85]. A similar trend was observed by Han et al. [86] for $MoO_{3-\delta}$ films prepared using thermal evaporation. It is suggested that the relative amount of Mo^{5+} states exhibits a minimum for films annealed at 200 °C, i.e., composition $MoO_{2.75}$. Note that, in most cases, the oxidation state of Mo^{4+} was not detected except for films in which the MoO_2 phase co-exists with α-MoO_3.

Recently, Novotny and Lamb [84] prepared MoO_x films deposited on α-Al_2O_3 (0001) at 580 °C using a conventional molecular-beam epitaxy Knudsen cell. The films deposited in a vacuum and in O_2 atmosphere at 580 °C were oxygen deficient with an average formula $MoO_{2.67}$. Their remarkable thermal stability is due to oxygen vacancies. For these films the XPS binding energies are recorded at 530.6 ± 0.1 eV for O 1s and 232.6, 231.0 and 229.2 ± 0.1 eV for Mo $3d_{5/2}$ peaks of Mo^{6+}, Mo^{5+} and Mo^{4+} oxidation states, respectively. Similar binding energies were obtained by Bhosle et al. [45] for $MoO_{2.75}$ films grown using the PLD method on sapphire substrates at 500–600 °C under O_2 pressure of 0.1 Pa. MoO_x films prepared using hot wire the oxidation-sublimation deposition (HWOSD) technique at room temperature under an oxygen pressure of 0.2 Pa were amorphous. XPS analysis showed that the composition $MoO_{2.94}$ and

the oxygen vacancies led to an electrical conductivity of 1.6×10^{-6} S cm^{-1} [87]. XPS studies of the MoO_x (x = 2.64–2.73) films fabricated using RF reactive magnetron sputtering with various oxygen flow rates (1.6–3.6 sccm) under pressure fixed at 0.4 Pa indicated the presence of Mo^{5+} and Mo^{6+} oxidation states and excluded the presence of Mo^{4+} states [88]. These films are semiconductors (n-type) in nature.

3.3. Morphology

The crystallite size (or coherent length) was determined from the full-width at half-maximum β_{0k0} of the (0k0) XRD reflections, using the Scherrer formula $L_c = K\lambda/\beta_{0k0}\cos\theta_{0k0}$. The average crystallite size varied between 23 and 69 nm in the T_s range 200–450 °C. Since surface roughness is an important physical parameter that affects the electrochemical performance, the surface topography was investigated using atomic force microscopy (AFM). Figure 8a shows the SEM image of the substrate surface. The typical surface morphology of a PLD $MoO_{3-\delta}$ films grown under P_{O2} = 13 Pa was investigated using AFM imaging (Figure 8b–d). The AFM results showed that the root-mean-square (RMS) roughness varies from 1.2 to 4.8 nm for the film deposited in the T_s range 100–400 °C. The growth temperature dependence of the grain size is plotted in Figure 9. It is observed that, in the range 100–500 °C, the grain size follows an exponential law with T_s. The surface roughness of films formed at emphT_s = 450 °C, i.e., $0.85Mo_8O_{23}$-$0.15MoO_3$, is about 7.2 nm, which is consistent with the XRD data. This is in contrast with the results reported by Hussain et al. [43]. They determined a surface roughness of 3.4 nm for crystalline MoO_3 films deposited using PLD at 200 °C under P_{O2} of 10 Pa and concluded that the surface roughness of the films decreased and the grain size increased with the increase in T_s. The different behavior is attributed to high stress in the films generated by the growth of films on substrate with different textures (amorphous, crystallized, textured, metallic) [31]. Fernandes-Cauduro et al. [85] studied the effect of oxygen partial pressure and sputtering power on amorphous DC-sputtered MoO_x films. It was found that the surface roughness (R_{rms}) was calculated from AFM relative height profiles for the as-deposited films on commercial ITO decreased from 2.2 to 1.0 nm, when the P_{O2} increased from 0.1 to ~0.3 Pa.

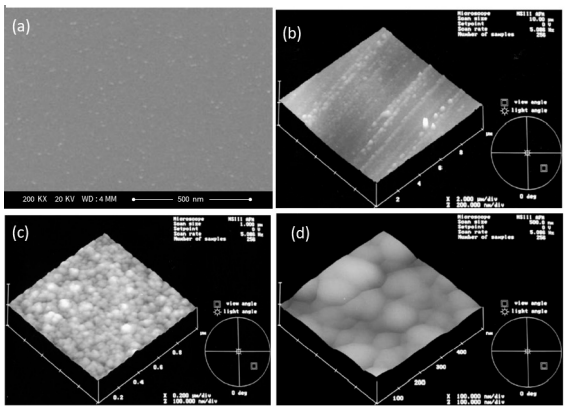

Figure 8. (**a**) SEM image of the substrate surface. (**b**–**d**) AFM images of $MoO_{3-\delta}$ films grown using the PLD technique at 25, 300 and 450 °C under P_{O2} = 13 Pa, respectively.

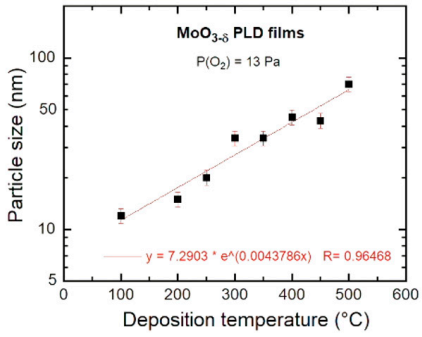

Figure 9. Particle size of $MoO_{3-\delta}$ films as a function of the deposition temperature.

3.4. Electrochemical Properties

Figure 10 shows the galvanostatic discharge-charge profiles of the $MoO_{3-\delta}$ thin-film electrodes vs. Li^+/Li at a current rate of 1 A g^{-1} (~1C) in the potential window 3.0–0.05 V. For all electrodes, the voltage dropped from the open-circuit voltage (OCV) of ~3.0 V during lithiation to reach firstly a small pseudo-plateau at ca. 2.4 V and secondly a large plateau at ca. 0.4–0.5 V. During the charge process, the voltage curve displays a smooth slope region with a loss of capacity. The charge-discharge curves of $MoO_{3-\delta}$ thin films display a similar S-shape. For all samples, we observe that the first charge capacities are lower than the first discharge capacities. After the first cycle of cell formation, the charge capacities stabilized. A large irreversible capacity decay of the first cycle is commonly observed for the transition-metal oxides because of the formation of the solid electrolyte interphase (SE)I layer and the irreversible phase transformation [89–92].

The electrochemical activity for Li^+ storage of the oxygen-deficient oxides occurs with various degrees of Li^+-ion uptake; the initial discharge specific capacity varied between 390 and 484 μAh cm^{-2} μm^{-1}. For thin-film electrodes, the specific capacity is generally expressed as volumetric capacity (μAh cm^{-2} μm^{-1}) due to the inaccuracy of the weight and density. Table 2 summarizes the electrochemical characteristics of the different $MoO_{3-\delta}$ thin film electrodes, i.e., specific discharge capacity of the 1st and 2nd discharge, Coulombic efficiency (CE) and specific capacity after 100 cycles. The initial CE of $MoO_{3-\delta}$ thin film anodes remains almost at ~75% irrespective of the deposition temperature. The high reversible capacity of the $MoO_{2.894}$ electrode (~484 μAh cm^{-2} μm^{-1}), which corresponds to the insertion of ~5.78 Li^+/Mo, is close to the theoretical maximum (5.79 Li^+/Mo). After 100 cycles performed at a 1 A g^{-1} rate, this film delivers a specific capacity of 300 μAh cm^{-2} μm^{-1} (~670 mAh g^{-1}). The irreversible insertion is largest for the electrode $MoO_{2.982}$, which can be attributed to its low conductivity. Note that the theoretical specific capacity of 1117 mAh g^{-1} (6 Li per Mo) corresponds to a volumetric capacity of 5026 mAh cm^{-3} (taking a density of 4.5 g cm^{-3}), which is equivalent to 502.6 μAh cm^{-2} μm^{-1} for MoO_3 thin film.

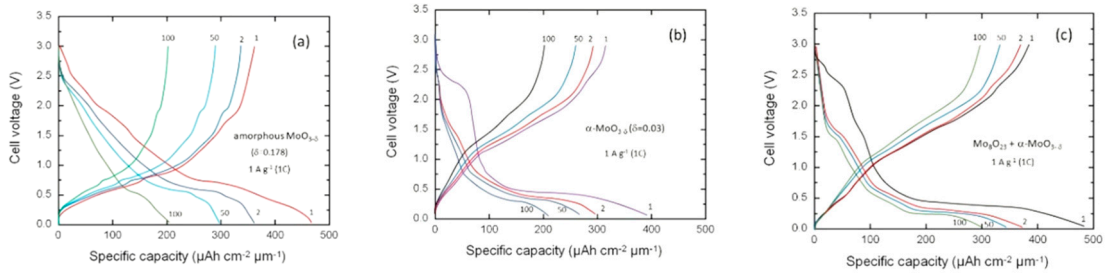

Figure 10. Galvanostatic discharge-charge profiles of Li//Mo-O thin films recorded at 1 A g^{-1} current density in the voltage range 3.0–0.05 V. (**a**) Amorphous $MoO_{3-\delta}$ film deposited at 25 °C, (**b**) $MoO_{3-\delta}$ film deposited at 200 °C and (**c**) $0.85Mo_8O_{23}$-$0.15MoO_3$ film deposited at 450 °C.

Table 2. Electrochemical characteristics of $MoO_{3-\delta}$ thin film anodes. Data were collected at a current density of 1 A g^{-1} in the potential window 3–0.05 V.

Electrode	Specific Discharge Capacity (μAh cm^{-2} μm^{-1})		CE (%)	Specific Capacity after 100 Cycles (μAh cm^{-2} μm^{-1})
	1st	2nd		
$MoO_{2.822}$	468	362	0.77	205
$MoO_{2.982}$	390	295	0.74	209
$MoO_{2.884}$	484	372	0.77	300

In the potential window 3–0.05 V, the lithiation in MoO_3 is believed to take place in two stages. Stage I occurs up to a potential of 1.5 V, in which Li^+ ions intercalate with the orthorhombic framework to form a solid solution according the relation:

$$MoO_{3-\delta} + xLi^+ + xe^- \rightarrow Li_xMoO_{3-\delta} \quad (2)$$

In Li_xMoO_3 (Li bronze phase), the inserted lithium content ranges between 1.0 and 1.5, up to a potential of 1.5 V [93]. The Li^+ ions are accommodated in the interlayer spacing between octahedral basal Mo−O layers and can be reversibly extracted. The oxidation state of Mo in Li_xMoO_3 decreases with x from +6 to about +4.5 leading to a corresponding fall in enthalpy of insertion. The stage II corresponds to potentials below 0.7 V, for which the further lithiation of Li_xMoO_3 occurs by a mechanism of conversion. The full reduction is expressed by the relation [94]:

$$Li_xMoO_{3-\delta} + (6 - x - \delta)Li^+ + (6 - x - \delta)e^- \rightarrow (3 - \delta)Li_2O + Mo \quad (3)$$

During charge following the full conversion reaction, the extracted Mo metal is re-oxidized by Li_2O. In the potential range below 0.7 V vs. Li^+/Li, the discharge process is a conversion reaction occurring at ca. 0.2 V (Equation (3)); the reduction action of Mo^{4+} to metallic Mo^0 occurs near 0.2 V. Li reacts with the $Li_xMoO_{3-\delta}$ solid solution to form nano-scaled metallic particles nano-dispersed in a Li_2O matrix. The reversibility of Li_2O is due to the presence of nano-scaled Mo^0 particles [95]. Note that MoO_3 nanoparticles and films present similarly continuous and smooth discharge curves, unlike the bulk material which does not show significant capacity in the low-potential range. The primary reason for Coulombic efficiencies of ~77% is the reversibility of Li_2O in lithiated $MoO_{3-\delta}$ thin films studied here.

Figure 11a,b shows the incremental capacity (IC) profiles, i.e., differential capacity (dQ/dV) vs. cell voltage, of the first lithiation-delithiation process in α-$MoO_{3-\delta}$ and $0.85Mo_8O_{23}$-$0.15MoO_3$ thin films deposited at 450 °C. This analysis can be considered as an efficient tool to determine the electrochemical spectroscopy of electrodes [96]. For instance, IC has been successfully applied to analyze the behavior of doped or blended cathodes [97]. The IC curves were extracted from the galvanostatic charge-discharge (GCD) profiles (Figure 8c) to further characterize the electrochemical lithium insertion and extraction processes showing the transformation after the first lithiation process. Each plot displays broad peaks in the voltage range of 0.05–3.0 V corresponding to the plateaus in GCD curves, related to the redox reactions. These results show clearly the peaks occurring in the first cathodic scan at 2.28, 1.36 and 0.41 V, which indicates the initial Li^+-ion insertion reaction given in Equation (2) and the strong peak at ca. 0.41 V corresponding to the conversion reaction expressed in Equation (3). The cathodic peak at 2.28 V is attributed to the irreversible phase transformation from α-$MoO_{3-\delta}$ to $Li_{0.25}MoO_{3-\delta}$ [42,98,99]. Iriyama et al. [42] reported a TEM analysis of the two-phase reaction in electrochemical lithium insertion within α-Li_xMoO_3 ($0 \leq x \leq 0.25$). The cyclic voltammogram exhibited a sharp peak at 2.77 V in the cathodic potential scan, which has no corresponding redox peak in the anodic scan, indicating the irreversibility of this reaction. As shown in Figure 9, the cathodic peak of the two-phase reaction occurs at lower potential (~2.30 V) due to the sub-stoichiometric composition of our films. The potential peaks in the first anodic scan (delithiation process) occurs at 1.20 and 1.72 V for α-$MoO_{3-\delta}$ thin films. The conversion peak shifts slightly toward a lower voltage for the mixed $0.85Mo_8O_{23}$-$0.15MoO_3$ thin film, which results in more reduced $MoO_{3-\delta}$. This oxygen-deficiency effect was also reported by Jung et al. [94]. Note that the anodic peaks are broad, which is indicative of the nano-size effect of pulverized Mo metallic particles after the full conversion process.

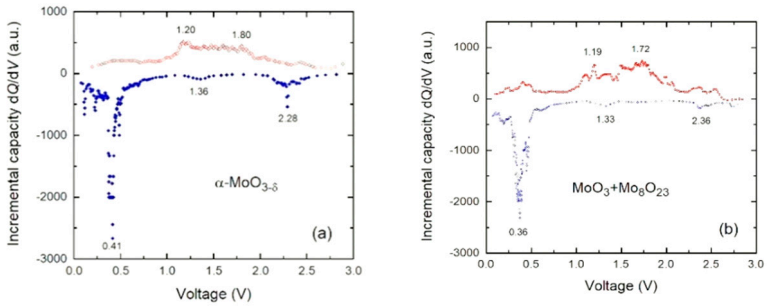

Figure 11. Incremental capacity curves (dQ/dV) vs. V of the first lithiation-delithiation cycle for (**a**) α-$MoO_{3-\delta}$ and (**b**) $0.85Mo_8O_{23}$-$0.15MoO_3$ thin film.

Figure 12 compares the cycling performance of oxygen deficient thin films. The rate capability (Figure 12a) was investigated at different current densities in the range 10–1000 mA g^{-1}. The $0.85Mo_8O_{23}$-$0.15MoO_3$ thin film exhibits significantly enhanced capacity retention. Figure 12b presents the discharge capacity with cycling at a current rate of 1 A g^{-1} over 100 cycles in the potential window 0.05–3.0 V for the three PLD thin films. For the amorphous a-$MoO_{3-\delta}$ film, the discharge capacity drops rapidly at the rate of 0.43% per cycle, while the discharge capacities of α-$MoO_{3-\delta}$ and $85Mo_8O_{23}$-$0.15MoO_3$ films decrease slowly at the rate of 0.19% per cycle. The remarkable cycling performance of the mixed $85Mo_8O_{23}$-$0.15MoO_3$ film is not only due to the higher electronic conductivity induced by oxygen vacancies but also benefits from the blend material composed of the layered MoO_3 and the quasi-1D Mo_8O_{23} suboxide. In comparison with the ratio of the discharge capacity at 0.01C and 1C rate, $Q_{1C}/Q_{0.01C}$ (Figure 12a) is found to be 67%, 78% and 76% for a-MoO_3, α-MoO_3 and $0.85Mo_8O_{23}$-$0.15MoO_3$ thin films, respectively, which suggests a better Li^+ ion kinetics in the layered α-MoO_3 material.

The evolution of the surface morphology of α-$MoO_{3-\delta}$ thin films after electrochemical cycling has been investigated using scanning electron microscopy. Figure 13 represents the SEM images of the structural properties of the film at the 5th and 50th cycle. It is remarkable that the film surface is maintained after 50 charge-discharge cycles. This picture corroborates the good cyclability of the α-$MoO_{3-\delta}$ thin films deposited at 300 °C, showing a small capacity decay upon cycling.

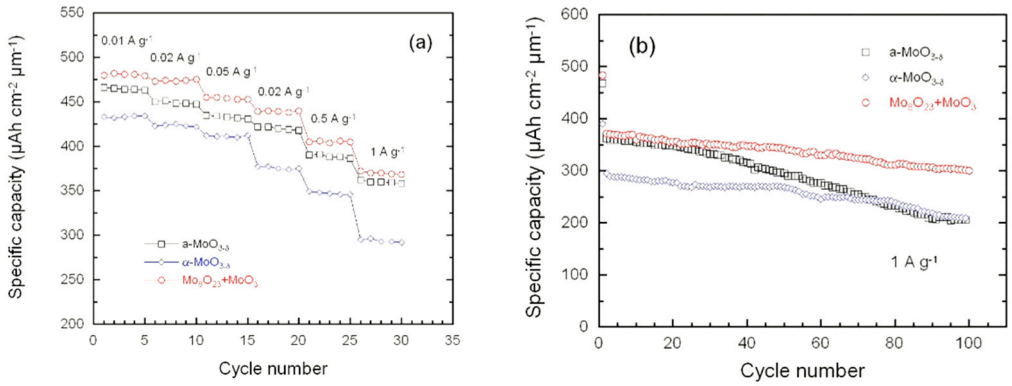

Figure 12. (**a**) Rate capability and (**b**) cyclability of $MoO_{3-\delta}$ film in Li cells with 1 mol L^{-1} $LiPF_6$ dissolved in ethylene carbonate and dimethyl carbonate (EC:DMC; 1:1 *w*/*w*) as aprotic electrolyte.

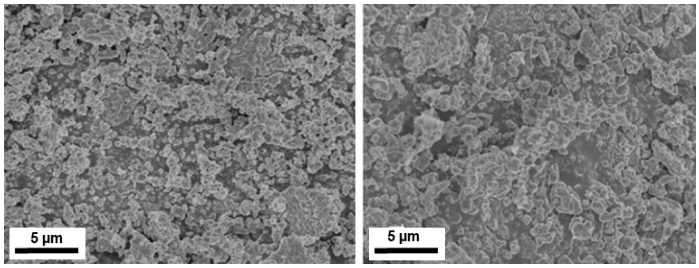

Figure 13. SEM images of the structural properties of the α-$MoO_{3-\delta}$ thin film electrode at (**left**) the 5th and (**right**) 50th cycle.

The chemical diffusion coefficients of Li^+ ions in the thin film frameworks were evaluated using the potentiostatic intermittent titration technique (PITT). The theoretical and experimental aspects of the kinetic behavior of metal-like anode materials, i.e., Li-alloys Li_xAl or $Li_{1+y}Sb$, have been extensively studied by Weppner and Huggins [100,101] and further applied to guest ions in insertion electrodes [102,103]. In mixed-conducting electrodes, the apparent chemical diffusion for Li^+ ions, D_{Li}, is the product ($D_{Li} = D_0\, W$) of the component diffusion D_0 by the enhancement factor (or thermodynamic factor) $W = (\partial \ln a_{Li}/\partial \ln c_{Li})$. Note that D_0 is an intrinsic property of the material and W_{TF} of thin film differs from W_B of the bulk due to the difference in the activity of intercalant species [104]. From the

point of view of fundamental studies, the use of thin film electrodes has the advantage of evaluating accurately intrinsic ion transport with known electrode surfaces by eliminating organic binders and conductive additives. The thermodynamic factor can be estimated from the gradient of the open-circuit voltage vs. composition ($\partial E/\partial x$) as:

$$W = \frac{\partial \ln a_{Li}}{d \ln c_{Li}} = \frac{xF}{RT}\frac{\partial E}{\partial x}. \quad (4)$$

In PITT, a transient current (I_t) is recorded within a very small potential step. The local current depends on the concentration gradient at the particle surface using Fick's first law. The time-dependent electric transient current I_t at each potential step obeys the following relation [b]:

$$I_t = \frac{2FA\Delta c_{Li} D_{Li}}{L} \exp\left(\frac{-\pi D_{Li} t}{4L^2}\right), \quad (5)$$

where F is the Faraday constant, A the surface area of the electrode, L the film thickness and $\Delta c_{Li} = c_s - c_0$ the difference of Li^+ concentration at the surface at time t and at time $t = 0$ during each potential step. The primary diffusion parameter is the characteristic diffusion time τ, which is defined for the one-dimensional case as $\tau = L^2/D_{Li}$. At short time ($\tau << L^2/D_{Li}$), the exponential term reduces to unity and the I_t obeys the Cottrell's equation:

$$I_t = \frac{2FA\Delta c_{Li} D_{Li}^{1/2}}{\pi^{1/2}} t^{-1/2} \quad (6)$$

In Figure 14a, the curve I_t vs. $t^{-1/2}$ shows a linear part with a slope proportional to the square root of the diffusion coefficient. This part shows primarily a finite-length diffusion behavior due to the interfacial charge-transfer and ohmic potential drop [105,106]. In the long-term domain, Equation (5) can be linearized by taking its logarithmic form:

$$\ln I_t = \ln\left(\frac{2FA\Delta c_{Li} D_{Li}}{L}\right) - \frac{\pi^2 D_{Li}}{4L^2} t. \quad (7)$$

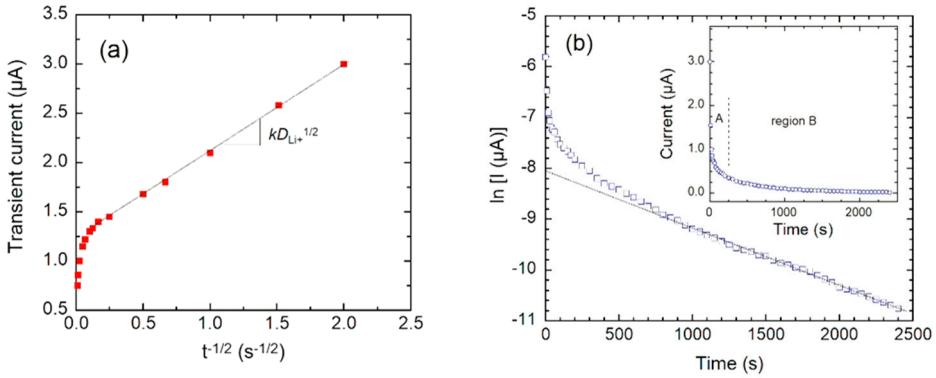

Figure 14. Time-dependent transient current showing the typical potentiostatic intermittent titration technique (PITT) response for PLD α-$MoO_{3-\delta}$ films, (**a**) at short time ($\tau << L^2/D_{Li}$) and (**b**) at long time ($\tau >> L^2/D_{Li}$).

This equation describes the semi-infinite planar diffusion in the film and satisfies the condition $\tau >> L^2/D_{Li}$. The time differentiation of this equation gives:

$$D_{Li} = \frac{4L^2}{\pi^2}\frac{\partial \ln I_t}{\partial t}, \quad (8)$$

which allows the determination of the apparent diffusion coefficient from the slope of the linear region of the ln(I_t) vs. t plot as shown in Figure 14b [96].

Figure 15a presents the typical variation of the thermodynamic factor against the cell voltage (W vs. E) calculated from the 2nd discharge response of a Li//α-$MoO_{3-\delta}$ cell using Equation (4). The average value of W at E = 0.5 V is listed in Table 3. As expected for a metal oxide, W is in the range 20–30 [104]. Figure 15b compares the D_{Li} values for PLD $MoO_{3-\delta}$ films in direct contact with the aprotic electrolyte. Note that the curves D_{Li} vs. cell voltage have the same features as two minimum values at 0.5 and 1.9 V. The results summarized in Table 3 show that the α-$MoO_{3-\delta}$ thin film deposited at T_s = 300 °C exhibits the higher diffusion coefficient in the range from 4×10^{-14} to 6×10^{-12} cm^2 s^{-1}. This high value is due to the layered-like structure of α-$MoO_{3-\delta}$, inducing larger open Li sites and favorable transport paths during the discharge-charge processes.

Table 3. Calculated D_{Li}+ values of a-MoO_3, α-MoO_3 and 0.85Mo_8O_{23}-0.15MoO_3 thin film anodes from the PITT experiments.

Thin Film Anode	D_{Li}+ (cm^2 s^{-1})		W @ 0.5 V
	min	max	
a-$MoO_{3-\delta}$	2×10^{-15}	7×10^{-14}	34.5
α-$MoO_{3-\delta}$	4×10^{-14}	6×10^{-12}	21.8
0.85Mo_8O_{23}-0.15MoO_3	7×10^{-15}	1.1×10^{-12}	25.2

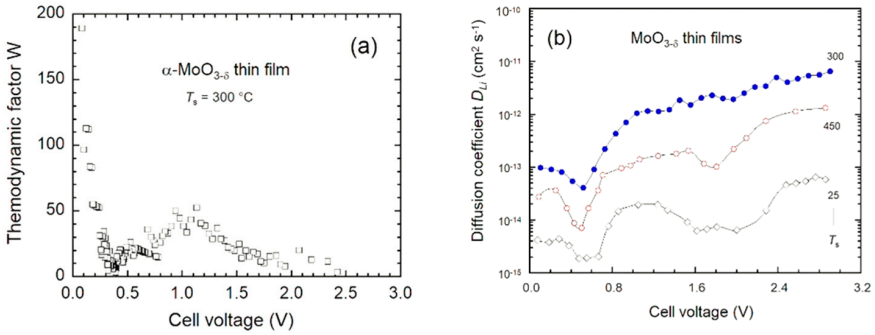

Figure 15. (**a**) Typical curve W vs. E for a α-MoO_3 thin film. (**b**) Apparent Li^+ ion diffusion coefficients vs. cell voltage determined from PITT measurements for a-MoO_3, α-MoO_3 and 0.85Mo_8O_{23}-0.15MoO_3 thin films deposited at 25, 300 and 450 °C, respectively.

4. Discussion

4.1. Growth Conditions

These results shed light on the growth process of the oxygen-deficient $MoO_{3-\delta}$ films prepared via different PLD conditions. The ability to generate these films with various compositions and morphologies is the most significant result of this work. The successful manufacture of sub-stoichiometric films has been optimized by the adjustment of the PLD growth parameters in order to obtain the best electronic properties and the best electrochemical properties for their potential application as electrodes for lithium microbatteries; the growth process of $MoO_{3-\delta}$ films has been discussed several times [4,43–46]. Ramana and Julien [4] suggested that creation of oxygen vacancies in deposited $MoO_{3-\delta}$ film is due to the re-evaporation from the surface of the substrate. In this process, energy levels in the energy gap are generated close to the valance band (E_v) considered as donor centers. It is widely recognized that α-$MoO_{3-\delta}$ films prepared at low temperature (T_s < 100 °C) are ill-textured and highly disordered with an amorphous contribution. Zhang et al. [50] reported that ITO/spin-coated $MoO_{2.98}$ films are amorphous and exhibit a deep-blue color. The influence of the partial O_2 pressure was discussed by several workers. Carcia and McCarron showed the influence of the partial O_2 pressure on the structure of magnetron-sputtered MoO_3 films. Using a total

argon plus oxygen pressure of 1.3 Pa, α-MoO_3 grew under P_{O_2} = 50%, whereas β-MoO_3 (monoclinic structure) was formed under P_{O_2} ≈ 10% [107]. Similarly, Altman et al. [108] fabricated MoO_3 thin films using a molecular beam epitaxy technique assisted by oxygen plasma under a low O_2 pressure of 4 mPa. By manipulating the deposition conditions, i.e., temperature, deposit cycle and deposition rate, epitaxial β-MoO_3 (tetragonal phase) thin films were grown on $SrLaAlO_4$ substrates at 400 °C, while the decrease of the deposition temperature to 260 °C resulted in the formation of polycrystalline α-MoO_3 (orthorhombic phase) films. To obtain suboxide $MoO_{2.86}$ thin films using reactive magnetron sputtering at room temperature, the O_2 ratio of 15% was fixed in the Ar + O_2 gas mixture at a total pressure of ~1 Pa [34]. The band-gap E_g of 2.82 eV was reported for $MoO_{2.86}$ film (200 nm thick). For 30% O_2, a stoichiometric MoO_3 film was prepared. Siokou et al. obtained suboxide $MoO_{2.78}$ films by heat treatment at 300 °C for 3 h in vacuum of stoichiometric MoO_3 films (colorless) thermally evaporated on (In_2O_3:Sn)-coated glass sheets. The deep blue color of $MoO_{2.78}$ is associated to a continuous distribution between +6 and +5 Mo states [109].

When prepared at high temperature (T > 400 °C), oxygen-deficient Mo-O oxides crystallized as a mixture of stoichiometric MoO_3 with a Magnéli-type phase, i.e., Mo_4O_{11}, Mo_8O_{23}, $Mo_{17}O_{47}$, etc. Ressler et al. [110] observed the formation of crystalline Mo_4O_{11} at temperatures higher than 500 °C. At 500 °C, Anbananthan reported the formation of a lower valent Mo-O oxide, namely the Mo_4O_{11} phase, for an MoO_3 electrode deposited on TiO_2 foil. It was demonstrated that the Mo_4O_{11} layer promoted the electrochemical Fe^{3+}/Fe^{2+} reaction [111]. Hashem et al. synthesized 200 nm-thick oxygen deficient Mo_xO_y particles, formed using a blend of α-MoO_3 and γ-Mo_4O_{11} [112]. The composition 0.65MoO_3-0.35Mo_4O_{11} was obtained by calcination of the precursor (ammonium heptamolybdate tetrahydrate as a source of Mo) heat treated with a small fraction of zirconia under reduced atmosphere at 500 °C for 5 h in a 5% H_2/Ar flow. Defective MoO_x films grown on glass substrate at 300 °C using spray pyrolysis have been identified as Mo_9O_{26} phase. After annealing at 500 °C for 20 h in a controlled O_2 atmosphere, the XRD patterns of the heat-treated films showed the presence of two crystallographic phases: monoclinic Mo_9O_{26} and orthorhombic $Mo_{17}O_{47}$. The Mo_9O_{26} phase grew preferentially along the (712) plane [113].

4.2. Electronic Properties

MoO_3 is known to be an unintentional *n*-type semiconductor at ambient conditions, due to intrinsic point defects related to oxygen vacancies (V_O) and molybdenum interstitials (Mo_i) [13]. It has been widely recognized that the introduction of oxygen vacancies (V_O) is an efficient strategy to promote the specific discharge capacity and rate capability and to boost the Li^+-ion diffusion of electrode materials [15–20]. Enhancement of the attainable capacity is attributed to extra valence electrons into the delocalized electron cloud. Similarly, in TiO_2, due to oxygen vacancies, a narrowed bandgap and change of the Fermi energy level indicates an increase of electron concentration [114]. Recently, it has been demonstrated that anion vacancies in insertion electrode materials can improve the energy storage capacity and reduce the insertion energy and ion diffusion barrier in the host lattice [27,115–120].

Figure 16 presents a diagram of the band structure close to the surface of $MoO_{3-\delta}$ film. Because of the oxygen vacancies, the Fermi level is enhanced and the concentration of electrons in the conduction band is increased [86]. The increase of Mo^{5+} (reduction of the O/Mo ratio) induces a decrease of the surface dipole lowering the work function φ (φ ≈ 5.95 eV for T_s = 450 °C). The large work function of $MoO_{3-\delta}$ films is attributed to its closed-shell character and the lowered electrostatic potential of the inner Mo-O units due to the dipole layer created by planes of terminal oxygen (O_1) sites. Therefore, the oxygen vacancy is a shallow donor, the reason why $MoO_{3-\delta}$ easily becomes a n-type degenerate semiconductor [121,122]. Julien et al. also suggested a decrease in optical band gap and attributed the decrease to the formation of oxygen-ion vacancies. The energy gap of $MoO_{3-\delta}$ films is located between 2.8 and 3.2 eV depending on the substrate and annealing temperature [31].

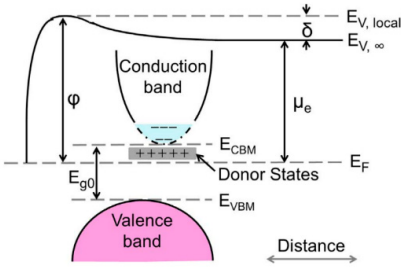

Figure 16. Band structure diagram near the $MoO_{3-\delta}$ film surface. E_F, E_{g0}, E_{CBM}, E_{VBM}, φ, μ_e, $E_{V,local}$ and $E_{V,\infty}$ represent the Fermi level, intrinsic band gap, conduction band minimum, valence band maximum, work function, electron chemical potential, local vacuum level and absolute vacuum level, respectively. Reproduced with permission from [86]. Copyright 2018 Elsevier.

4.3. Electrochemistry

Orthorhombic α-MoO_3 is an attractive transition-metal oxide as an anode material for Li-ion batteries, owing to its unique layered structure and its high theoretical Li uptake consequently to the high oxidation state (+6) of Mo. It has a theoretical specific capacity of 1117 mAh g^{-1} based on the full conversion reaction in deep discharge voltages, which is higher than MoO_2 (838 mAh g^{-1}). The empty interlayer channels formed by its double-layered structure built from MoO_6 octahedra provide rapid accommodation of Li ions. However, the insulating nature of α-MoO_3 (band gap of 3.1 eV) and the structural degradation associated to the conversion reaction prevent its utilization as an anode [123]. To overcome this drawback, the design of a material with an oxygen-deficient lattice is the key issue to increase the electronic conductivity by several orders of magnitudes. Moreover, the use of hierarchical nano-structures also helps. Indeed, the implementation of a carbon-free $MoO_{3-\delta}$ electrode is possible due to the enhanced electronic transport in oxygen-deficient oxides and the reduction of the Li^+-ion pathway in nano-structured materials.

Few studies report the electrochemical features of Mo-oxide thin film anodes, which in contrast with traditional electrodes did not use conductive additive and binder [124,125]. Amorphous films (a-MoO_x, $2 < x < 3$) were prepared using a reactive magnetron sputtering carried out at power of 60 W under a working pressure of 0.8 Pa and total gas flow rate at 40 sccm (Ar + O_2 of 80:20) [125]. a-MoO_x films are a mixture of MoO_2 and MoO_3 phase (O/Mo ≈ 2.75) and have the morphology of cauliflower-like protuberances, which consist of ultra-fine particles. After 100 discharge-charge cycles at a current density of 90 μA cm^{-2} (~225 mA g^{-1}) in the potential window 0.01–3.0 V, the specific capacity was 315 μAh cm^{-2} μm^{-1} (mass loading of 0.45 mg). Porous α-MoO_3 films were fabricated using electrodeposition on Ni foam substrates. These films are composed of grains of several tens of nm in size with nanoholes of the same size [123]. After 50 cycles, the Li^+ insertion/extraction capacity and the Coulombic efficiency of the thin-film electrode was tested at a current density of 3 A g^{-1} are 650 mAh g^{-1} and 97%, respectively. The smaller grain size and widespread nanoholes lead to high Li^+ insertion kinetics with a diffusion coefficient of 7.1×10^{-11} cm^2 s^{-1}, obtained from EIS measurements.

In the following, we compare our results with the electrochemical performance of nanostructured MoO_3 anodes. The state of the art of MoO_x suboxide anodes is summarized in Table 4 [94,123–138]. Oxygen-deficient MoO_x nanosheets (NSs, 20–30 nm thick) prepared by oxidation of Mo powders in H_2O_2 were investigated as anode materials in Na-ion batteries and compared to the MoO_3 counterpart [134]. XPS analysis showing equal amounts of Mo^{6+} and Mo^{5+} cations providing particles with a composition $MoO_{2.75}$ (Mo_4O_{11}) formed by close staking of 20–30 nm thin flakes (nanosheets, NSs) when they are prepared using a polymer-assisted solvothermal method [133]. Remarkable electrochemical performances were obtained for NSs, which delivered a specific capacity of 179 mAh g^{-1} at 1 A g^{-1} rate after 100 cycles. The advantage of oxygen deficiency in MoO_3 is clearly demonstrated by the better Li^+ ion transport with a diffusion coefficient of 4.36×10^{-11} cm^2 s^{-1} for intense blue colored $MoO_{2.75}$ against 8.28×10^{-12} cm^2 s^{-1} for white MoO_3. Oxygen-deficient Mo_4O_{11} ($MoO_{2.75}$) exhibits better transport properties than MoO_3, i.e., small electrical resistivity $\rho \approx 10^{-4}$ Ω cm and a Li-ion diffusion coefficient of

~4×10^{-12} cm^2 s^{-1}. Moreover, it can accommodate up to 2.1 Li^+/Mo in the potential range 3.6–1.5 V vs. Li^+/Li, providing a theoretical specific capacity of 401 mAh g^{-1} [135]. However, the reversible capacity becomes stable at the level of 170–200 mAh g^{-1} [136]. MoO_3 nano-spheres (20–30 nm in diameters) were synthesized using electrophoresis deposition on a stainless-steel substrate. When cycled between 3.0 and 0.005 V at a C/2 rate, they delivered an initial discharge capacity of ~630 mAh g^{-1} (3.4 Li^+ per Mo inserted reversibly uptake) with no capacity degradation after 150 cycles [132]. The same group of searchers fabricated MoO_x nanoparticles using hot-wire chemical vapor deposition (HWCVD) under Ar + O_2 gas mixture at reactor pressures in the range 35–150 Torr consisting of a mixture of crystalline MoO_2 + α-MoO_3 + β-MoO_3 phases, but electrodes using acetylene black and polyvinylidene fluoride (PVdF) were not free binder [129,131].

The effect of annealing temperature on electrochemical performance of MoO_x nanospheres was studied using binder-rich electrodes. The whitish-blue (indicative for x close to 3) particles deliver a capacity of ~800 mAh g^{-1} after 40 cycles [131]. MoO_3 nanobelts synthesized using a simple hydrothermal route and heat-treated at 265 °C for 3 h in air exhibit an initial discharge capacity of 1250 mAh g^{-1} being cycled at a current rate of 0.1 C and an initial Coulombic efficiency of 67% [137]. Jung et al. prepared partially reduced Mo oxides, namely $MoO_{2.929}$, $MoO_{2.903}$ and $MoO_{2.895}$, by ball- milling as anode materials with 10% acetylene black. It is shown that the specific discharge capacity slightly increases with the increase of oxygen vacancy in the MoO_3 lattice. Remarkably, the $MoO_{2.895}$ anode can uptake 8Li per Mo in the potential range 0–3 V vs. Li^+/Li [94]. MoO_3 nanobelts synthesized using a simple hydrothermal route and heat-treated at 265 °C for 3 h in air exhibit an initial discharge capacity of 1250 mAh g^{-1} at a rate of 0.1C and an initial Coulombic efficiency of 67% [137]. Liu et al. reported an initial discharge capacity of 1200 mAh g^{-1} at 50 mA g^{-1} for a crystalline MoO_3 anode containing 15% acetylene black, which fell at ~320 mAh g^{-1} at the 10th cycle [138]. Ma et al. [139] investigated the electrochemical performance of suboxide-MoO_3 synthesized via a surfactant-assisted solvothermal route exhibiting an average valence state of 5.58 for Mo cations. The $MoO_{2.79}$ anode containing 15% acetylene black delivered a first discharge capacity of 760 mAh g^{-1} at 0.2 A g^{-1} rate. Wu et al. [128] reported a specific capacity up to 930 mAh·g^{-1} over 200 cycles for Mo-O anodes fabricated from slurry spread onto copper foils containing 20 wt.% acetylene black (conducting additive). According to the XRD pattern, the active material was a mixture of three phases, MoO_3 + Mo_4O_{11} + MoO_2, and the XPS analysis showed the valence state of Mo on the surface as 5.6. In summary, our pulsed laser deposited $MoO_{3-\delta}$ suboxide films exhibit high specific capacity and good stability due to the improved Li^+ diffusion kinetics [140,141] as compared with films fabricated using electrodeposition [124] and electron-beam evaporation [125].

Table 4. Comparison of the electrochemical performance of nanostructured anodes materials.

Material [a]	Particle Size (nm)	Electrochemical Performance	Ref.
$Mo_{17}O_{47}$ NWs	~90	630 mAhg^{-1} @ 50 mAg^{-1} for 20 cycles	[123]
MoO_3 NRs	100–250	460 mAhg^{-1} @ 1.5 Ag^{-1} for 50 cycles	[127]
$MoO_{2.895}$	~1000	600 mAhg^{-1} @ 0.03C for 35 cycles	[94]
MoO_3 NSs	5–20	630 mAhg^{-1} @ C/2 for 150 cycles	[132]
MoO_3 NRs	400	450 mAh g^{-1} @ 25 mA g^{-1} for 90 cycles	[126]
MoO_3 NSs [b]	40	800 mAh g^{-1} @ C/10 for 40 cycles	[131]
MoO_3 NBs	150	300 mAh g^{-1} @ C/10 for 50 cycles	[137]
MoO_3 NFs	20–30	550 mAh g^{-1} @ 2C for 75 cycles	[123]
MoO_3 NBs	150	300 mAh g^{-1} @ 50 mA g^{-1} for 10 cycles	[138]
MoO_3 NSs	~3–50	620 mAhg^{-1} @ C/2 for 150 cycles	[129]
α-MoO_3 NBs	~220	1067 mAhg^{-1} @ C/2 for 50 cycles	[130]
MoO_3	100–500	450 mAh g^{-1} @ 200 mA g^{-1} for 200 cycles	[128]
MoO_x	100–500	900 mAh g^{-1} @ 200 mA g^{-1} for 200 cycles	[128]
MoO_3 TF	100	650 mAh g^{-1} @ 3 A g^{-1} for 50 cycles	[124]
MoO_x TF	1.1 μm thick	347 μAh cm^{-2} @ 90 μA cm^{-2} for 100 cycles	[125]
a-$MoO_{2.822}$ TF	amorphous	205 μAh cm^{-2} $μm^{-1}$ @ 1 Ag^{-1} for 100 cycles	this work
α-$MoO_{2.982}$ TF	69	209 μAh cm^{-2} $μm^{-1}$ @ 1 Ag^{-1} for 100 cycles	this work
MoO_3 + Mo_8O_{23} TF	72	300 μAh cm^{-2} $μm^{-1}$ @ 1 Ag^{-1} for 100 cycles	this work

[a] NWs: nanowires, NRs: nanorods, NSs: nanospheres, NBs: nanobelts; NFs: nanoflakes; [b] electrode containing acetylene black and PVdF binder (70:20:10).

4.4. Li^+-ion Kinetics

The potentiostatic intermittent titration technique has been used successfully to study the lithium ion kinetics in planar $MoO_{3-\delta}$ thin films. The chemical diffusion coefficient is found to vary between 10^{-12} and 10^{-15} cm^2 s^{-1} in organic electrolyte. $D_{Li}{}^+$ differs by less than one order of magnitude for amorphous film with respect to crystallized films. This gives evidence that the diffusion of Li^+ ions changes importantly with the oxygen deficiency. For MoO_3 cathode films prepared using flash- and thermal-evaporation techniques at 250 °C, lithium diffusion coefficients are in the range 10^{-12}–10^{-11} cm^2 s^{-1} [141]. Halalay et al. determined D_{Li} of 10^{-11} cm^2 s^{-1} in amorphous MoO_3 films (550 nm thick) using an optical method relying on the application of the Beer-Lambert law [142]. In contrast, a low value of 2.88×10^{-21} cm^2 s^{-1} was reported for nano-composites formed using ultra-fine MoO_3 anchored in coal-based carbon fibers [143]. Ding et al. [144] fabricated $MoO_{3-\delta}$ nanorods (light blue color) through mechanical grinding of bulk powders, which show a diffusion coefficient of Li^+ ions of 3.2×10^{-14} cm^2 s^{-1} determined from an EIS experiment. The same amplitudes (1.35×10^{-14} cm^2 s^{-1}) were reported for MoO_3 nanobelts as anode materials [145]. MoO_3/amorphous carbon composite fabricated by calcinating polyaniline with ammonium heptamolybdate tetrahydrate exhibited a low Li diffusion coefficient of 3.4×10^{-14} cm^2 s^{-1} at room temperature [146]. Sun et al. [147] stated that oxygen vacancies in $MoO_{2.86}$ nanobelts promote a lower energy barrier for Li^+ diffusion but did not provide values. On the other hand, the oxygen deficient Mo_4O_{11} ($MoO_{2.75}$) exhibits better transport properties with an average lithium chemical diffusion coefficient of ~4.5×10^{-12} cm^2 s^{-1} [148].

These data can be compared with the previously reported values for metal-oxide thin films. $D_{Li}{}^+$ data measured using PITT for PLD $LiMn_2O_4$ (LMO) film vary in the range from 3×10^{-13} to 6×10^{-13} cm^2 s^{-1} in the voltage range 3.9–4.3 V [149]. Julien et al. disclosed $D_{Li}{}^+$ values of 1.5×10^{-12} and 8.0×10^{-12} cm^2 s^{-1} at 4 V with composition-dependent behavior for PLD LMO films deposited at 100 and 300 °C, respectively [150]. Xie et al. investigated the potential dependence of PITT $D_{Li}{}^+$ of the $LiFePO_4$ thin film, which varies in a range of 10^{-14} to 10^{-12} cm^2 s^{-1} [151].

From the results listed in Table 4, listing $D_{Li}{}^+$ observed for $MoO_{3-\delta}$-based thin film anodes, it is obvious that the apparent diffusion coefficients are strongly dependent on the structure and morphology of $MoO_{3-\delta}$ thin films. Generally, bulk materials are composed of secondary particles (agglomerates), which are interconnected nanoparticles (primary particles) forming a mesoporous architecture. The mesopores (few tens of nm in size) are the intraconnecting voids formed between randomly packed nanoparticles favoring the high surface area between the active material and the electrolyte and enhancing the transport pathway. In contrast, thin films are composed of grains linked through grain boundaries, which are amorphous in nature. The absence of mesoporosity makes Li ion transport into the crystallite (29 nm in size) of the $MoO_{3-\delta}$ film more difficult. Thus, the morphology (mesoporosity, surface area, surface roughness) is the key parameter for transport of Li^+ ions into the active material. Moreover, the apparent diffusion coefficient D_{Li} in thin films depends on the thermodynamic factor W_F, which differs from W_B of the bulk [99]. For films deposited at $T_s < 400$ °C, the variation of D_{Li} with the electrode potential exhibits a "W"-type behavior with two minimum regions at ca. 0.5 and 1.9 V, which are related to the strong attractive interactions between Li^+ ions and the host lattice [152]. This behavior is quite consistent with the one observed in Li_xSi anode [153]. As $MoO_{3-\delta}$ thin films are oxygen-deficient materials, the model of charge transport in internal defect material can be applied [154]. Defects are Li-interstitials, Li*, and conduction electrons, e', for example. It has been shown that, in a solid solution where no internal defect reactions occur, the thermodynamic factor is related to the defect concentration (if dilute defects exist). The large increase of W may be also associated with the decrease of the electronic mobility in Li_xMoO_3 film.

The diffusion coefficients of Li^+ ions obtained in PLD-prepared $MoO_{3-\delta}$ thin films can be compared with other anode materials [141,155–163] listed in Table 5. For cathode films prepared using flash evaporation (0.5–0.6 μm thick), D_{Li} values are strongly dependent on T_s and vary in the range 10^{-12}–10^{-11} cm^2 s^{-1} [141]. Zhao et al. [124] investigated the Li^+-ion kinetics in porous MoO_3 anode films (150 nm thick) prepared using electrodeposition in acid peroxo-polymolybdate electrolyte.

The Li^+ diffusion of 7.1×10^{-11} cm^2 s^{-1} is indeed facilitated by the widespread nanoholes (several tens of nm) and by the small grains on the scale of ~100 nm.

Table 5. Diffusion coefficients of Li^+ ions in some anode materials.

Material	Sampling	D_{Li} (cm^2 s^{-1})	Ref.
Li_xMoO_3	thin film	10^{-12}–10^{-11}	[141]
MoO_3/a-C	nanocomposite	3.4×10^{-14}	[149]
α-MoO_3	nanobelts	3.3×10^{-14}	[155]
MoO_3:Sn	doped nanobelts	7.3×10^{-13}	[155]
porous MoO_3	electrodeposited	7.1×10^{-11}	[124]
a-$MoO_{3-\delta}$	sputtered thin film	3.0×10^{-14}	[156]
$Li_{2.1}Si$	nanopowder 50 nm	4.0×10^{-13}	[153]
$Li_{2.7}Si$	nanopowder 50 nm	2.0×10^{-12}	[153]
$TiNb_2O_7$	ball-milled 1–5 μm	4.6×10^{-14}	[157]
$TiNb_6O_{17}$	ball-milled 1–5 μm	1.3×10^{-13}	[157]
a-Si:H	thin film	4.0×10^{-13}	[158]
$LiSiO_2$	DFT calculation	2.6×10^{-11}	[159]
a-$Li_{2.5}SiO_2$	ReaxFF calculation	1.0×10^{-13}	[160]
Li_xC_6	graphite FG-A	1.2×10^{-10}	[161]
$Li_1(H_{0.224}C)_6$	disordered carbon	6.0×10^{-15}	[162]
LiC_6 (50–250 mV)	artificial graphite	10^{-10}–10^{-12}	[163]
$Li_{1.16}V_{0.93}O_2$	atomistic modelling	7.5×10^{-10}	[164]
a-$MoO_{2.822}$	PLD thin film	2.0×10^{-15}–7.0×10^{-14}	this work
α-$MoO_{2.982}$	PLD thin film	6.0×10^{-14}–6.0×10^{-12}	this work

5. Conclusions

In this work, we showed that $MoO_{3-\delta}$ thin films were successfully fabricated using a PLD technique with good control of the oxygen deficiency. To the best of our knowledge, this is the first report on the correlation between the nanoscale structure of $MoO_{3-\delta}$ thin films and their electrochemical properties as anode in lithium microbatteries. The structural properties investigated using XRD, RS and FTIR spectroscopies showed that crystallized films can be formed with a wide range of deviation from stoichiometry (δ). The formation of lattice defects can be explained in terms of oxygen re-evaporation from the surface of the substrate during the PLD process. As-deposited Mo-O films at T_s = 25 °C are amorphous in nature and highly oxygen deficient. The decomposition of the XPS spectra reveals that the Mo 3*d* spectra can be well fitted by two 3*d* doublets in the form of a Gaussian function, corresponding to Mo in +6 and +5 oxidation states. The atomic ratio O/Mo shows a small amount of oxygen vacancies in $MoO_{3-\delta}$ films deposited at $T_s \approx 200$ °C; the Mo sub-states were suppressed, resulting in a further oxidation of the film. The O/Mo ratio reaches the value of 2.982 when the temperature was increased to 300 °C, and a nearly stoichiometric α-MoO_3 film resulted. Further increase of T_s (≈ 450 °C) produces a film with O/Mo = 2.894, which corresponds to the composition 0.85 Mo_8O_{23}-0.15MoO_3. The electrochemical test of the 0.15MoO_3-0.85Mo_8O_{23} film shows a specific capacity of 484 μAh cm^{-2} μm^{-1} after 100 cycles of charge-discharge at a constant current of 0.5 A cm^{-2} in the potential range 3.0-0.05 V. So far, it is the best result obtained with $MoO_{3-\delta}$ thin films. Studies of the lithium transport in $MoO_{3-\delta}$ thin film electrodes have shown that D_{Li} is influenced by the nanostructure, morphology, grain size and gain boundaries. The formation of well-defined channels between slabs of the MoO_3 structure provides facile ionic conduction pathways in crystallized films. These channels are ill-defined in films deposited at low temperatures. This is a typical trend between crystalline and disordered networks. For instance, a value $D_{Li} = 6 \times 10^{-12}$ cm^2 s^{-1} is obtained for PLD films deposited at 300 °C.

This work has shown the advantage of PLD films free of conducting additive and binder commonly used in the fabrication of electrodes (i.e., 10% carbon black and 10% PVdF), as the use of these electrochemically inactive substances degrades the specific gravimetric capacity of the electrode.

On other hand, the PLD technique has shown unique advantages for the formation of dense films, easy control of the growth rate and production of high purity films with good preservation of the target-phase stoichiometry. The main drawback of PLD films is their limited capacity due to the relative difficulty to grow thick films with good adhesion (as a consequence of the low energy of few eV of molecules falling on the substrate). However, some improvements can be expected by the fabrication of mixed electrodes (for example $MoO_{3-\delta}$ + MoO_2) or blended electrodes (for example TiO_2 + $MoO_{3-\delta}$), in which the electronic conductivity can be adjusted.

Author Contributions: Conceptualization, C.M.J. and O.M.H.; investigation, A.L.-N., C.V.R., M.C.-L., A.A.-G., A.H.; writing—original draft preparation, C.M.J.; writing—review and editing, C.V.R. and A.M.; supervision, C.M.J. and O.M.H. All authors have read and agreed to the published version of the manuscript.

Funding: This research received no funding.

Acknowledgments: One of us (CVR) acknowledge the support from the National Science Foundation (NSF) with NSF-PREM grant #DMR-1827745.

Conflicts of Interest: The authors declare no conflicts of interest.

References

1. Julien, C. Solid State Batteries. In *Handbook of Solid-State Electrochemistry*; Gellings, P.J., Bouwmeester, H.J.M., Eds.; CRC Press: Roca Raton, FL, USA, 1997; Chapter 11, pp. 371–406.
2. Julien, C.M.; Mauger, A.; Vijh, A.; Zaghib, K. *Lithium Batteries: Science and Technology*; Springer: Cham, Switzerland, 2016; pp. 120–124.
3. Ramana, C.V.; Atuchin, V.V.; Groult, H.; Julien, C.M. Electrochemical properties of sputter-deposited MoO_3 films in lithium microbatteries. *J. Vac. Sci. Technol. A* **2012**, *30*, 04D105. [CrossRef]
4. Ramana, C.V.; Julien, C.M. Chemical and electrochemical properties of molybdenum oxide thin films prepared by reactive pulsed-laser assisted deposition. *Chem. Phys. Lett.* **2006**, *428*, 114–118. [CrossRef]
5. Saravanakumar, B.; Shobana, R.; Ravi, G.; Ganesh, V.; Yuvakkumar, R. Preparation and electrochemical characterization of Mo_9O_{26} nanopowders for supercapacitors applications. *Nano-Struct. Nano-Objects* **2019**, *19*, 100340. [CrossRef]
6. Sunu, S.S.; Prabhu, E.; Jayaraman, V.; Gnanasekar, K.I.; Gnanasekaran, T. Gas sensing properties of PLD made MoO_3 film. *Sens. Actuators B* **2003**, *94*, 189–196. [CrossRef]
7. Dillon, A.C.; Mahan, A.H.; Deshpande, R.; Parilla, P.A.; Jones, K.M.; Lee, S.-H. Metal oxide nano-particles for improved electrochromic and lithium-ion battery technologies. *Thin Solid Films* **2008**, *516*, 794–797. [CrossRef]
8. Simchi, H.; McCandless, B.E.; Meng, T.; Boyle, J.H.; Shafarman, W.N. Characterization of reactively sputtered molybdenum oxide films for solar cell application. *J. Appl. Phys.* **2013**, *114*, 13503. [CrossRef]
9. Bullock, J.; Cuevas, A.; Allen, T.; Battaglia, C. Molybdenum oxide MoO_x: A versatile hole contact for silicon solar cells. *Appl. Phys. Lett.* **2014**, *105*, 232109. [CrossRef]
10. Jacieniak, J.J.; Seifter, J.; Jo, J.; Mates, T.; Heegeer, A.J. A solution-processed MoO_x anode interlayer for use within organic photovoltaic devices. *Adv. Funct. Mater.* **2012**, *22*, 2594–2605. [CrossRef]
11. Gesheva, K.A.; Ivanova, T.M.; Bodurov, G.K. APCVD transition metal oxides—Functional layers in smart windows. *J. Phys. Conf. Ser.* **2014**, *559*, 012002. [CrossRef]
12. Vasilopoulou, M.; Palilis, L.C.; Georgiadou, D.G.; Kennou, S.; Kostis, I.; Davazoglou, D.; Argitis, P. Barrierless hole injection through sub-bandgap occupied states in organic light emitting diodes using substoichiometric MoO_x anode interfacial layer. *Appl. Phys. Lett.* **2012**, *100*, 013311. [CrossRef]
13. Hanson, E.D.; Lajaunie, L.; Hao, S.; Myers, B.D.; Shi, F.; Murthy, A.A.; Wolverton, C.; Arenal, R.; Dravid, V.P. Systematic study of oxygen vacancy tunable transport properties of few-layer MoO_{3-x} enabled by vapor-based synthesis. *Adv. Func. Mater.* **2017**, *27*, 1605380. [CrossRef]
14. Kihlborg, L. The crystal structure of $Mo_{18}O_{52}$ and the existence of homologous series of structures based on MoO_3. *Ark. Kemi* **1963**, *21*, 443–460.
15. Magnéli, A. The crystal structures of Mo_9O_{26} (beta'-molybdenum oxide) and Mo_8O_{23} (beta-molybdenum oxide). *Acta Chem. Scand.* **1948**, *2*, 501–517. [CrossRef]
16. Kihlborg, L. Studies on molybdenum oxides. *Acta Chem. Scand.* **1959**, *13*, 954–962. [CrossRef]

17. Kihlborg, L. The crystal structure of $Mo_{17}O_{47}$. *Acta Chem. Scand.* **1960**, *14*, 1612–1622. [CrossRef]
18. Åsbrink, S.; Kihlborg, L. A study of the crystal symmetry and structure of orthorhombic Mo_4O_{11} by least-squares techniques. *Acta Chem. Scand.* **1964**, *18*, 1571–1573. [CrossRef]
19. Sato, M.; Onoda, O.; Matsuda, Y. Structural transitions in Mo_nO_{3n-1} (n = 9 and 10). *J. Phys. C Solid State Phys.* **1987**, *20*, 4763–4771. [CrossRef]
20. Inzani, K.; Grande, T.; Vullum-Bruer, F.; Selbach, S.M. A van der Waals density functional study of MoO3 and its oxygen vacancies. *J. Phys. Chem. C* **2016**, *120*, 8959–8968. [CrossRef]
21. Tahini, H.A.; Tan, X.; Lou, S.N.; Scott, J.; Amal, R.; Ng, Y.H.; Smith, S.C. Mobile polaronic states in α-MoO_3: An ab initio investigation of the role of oxygen vacancies and alkali ions. *ACS Appl. Mater. Interfaces* **2016**, *8*, 10911–10917. [CrossRef]
22. Inzani, K.; Nematollahi, M.; Vullum-Bruer, F.; Grande, T.; Reenaasb, T.W.; Selbach, S.M. Electronic properties of reduced molybdenum oxides. *Phys. Chem. Chem. Phys.* **2017**, *19*, 9232–9245. [CrossRef]
23. Mattinen, M.; King, P.J.; Khriachtchev, L.; Heikkilä, M.J.; Fleming, B.; Rushworth, S.; Mizohata, K.; Meinander, K.; Räisänen, J.; Ritala, M.; et al. Atomic layer deposition of crystalline molybdenum oxide thin films and phase control by post-deposition annealing. *Mater. Today Chem.* **2018**, *9*, 17–27. [CrossRef]
24. Vasilopoulou, M.; Douvas, A.M.; Georgiadou, D.G.; Palilis, L.C.; Kennou, S.; Sygellou, L.; Soultati, A.; Kostis, I.; Papadimitropoulos, G.; Davazoglou, D. The influence of hydrogenation and oxygen vacancies on molybdenum oxides work function and gap states for application in organic optoelectronics. *J. Am. Chem. Soc.* **2012**, *134*, 16178–16187. [CrossRef] [PubMed]
25. Hou, Y.; Wang, J.; Hou, C.; Fan, Y.; Zhai, Y.; Li, H.; Dang, F.; Chou, S. Oxygen vacancies promoting the electrocatalytic performance of CeO_2 nanorods as cathode materials for Li–O_2 batteries. *J. Mater. Chem. A* **2019**, *7*, 6552–6561. [CrossRef]
26. Kröger, M.; Hamwi, S.; Meyer, J.; Riedl, T.; Kowalsky, W.; Kahn, A. Role of the deep-lying electronic states of MoO_3 in the enhancement of hole injection in organic thin films. *Appl. Phys. Lett.* **2009**, *95*, 123301. [CrossRef]
27. Shin, J.Y.; Joo, J.H.; Samuelis, D.; Maier, J. Oxygen-deficient $TiO_{2-\delta}$ nanoparticles via hydrogen reduction for high rate capability lithium batteries. *Chem. Mater.* **2012**, *24*, 543–551. [CrossRef]
28. Kim, H.; Cook, J.; Lin, H.; Ko, J.S.; Tolbert, S.H.; Ozolins, V.; Dunn, B. Oxygen vacancies enhance pseudocapacitive charge storage properties of MoO_{3-x}. *Nat. Mater.* **2016**, *16*, 454–460. [CrossRef]
29. Akin, U.; Safal, H. Thickness dependence of dispersion parameters of the MoO_x thin films prepared using the vaccum evaporation technique. *J. Alloys Compd* **2015**, *647*, 146–151. [CrossRef]
30. Borah, D.J.; Mostako, A.T.T.; Saikia, P.K.; Dutta, P. Effect of thickness and post deposition annealing temperature on the structural and optical properties of thermally evaporated molybdenum oxide films. *Mater. Sci. Semicond. Process.* **2019**, *93*, 111–122. [CrossRef]
31. Julien, C.; Khelfa, A.; Hussain, O.M.; Nazri, G.A. Synthesis and characterization of flash-evaporated MoO_3 thin films. *J. Cryst. Growth* **1995**, *156*, 235–244. [CrossRef]
32. Sun, S.; Sun, Y.; Wen, J.; Zhang, B.; Liao, X.; Yin, G.; Huang, Z.; Pu, X. MoO_{3-x}-deposited TiO_2 nanotubes for stable and high-capacitance supercapacitor electrodes. *RSC Adv.* **2018**, *8*, 21823–21828. [CrossRef]
33. Mohamed, S.H.; Kappertz, O.; Ngaruiya, J.M.; Pedersen, T.P.L.; Drese, R.; Wuttig, M. Correlation between structure, stress and optical properties in direct current sputtered molybdenum oxide films. *Thin Solid Films* **2003**, *429*, 135–143. [CrossRef]
34. Wang, D.; Yang, R.; Wu, L.; Shen, K.; Wang, D. Band alignment of CdTe with MoO_x oxide and fabrication of high efficiency CdTe solar cells. *Sol. Energy* **2018**, *162*, 637–645. [CrossRef]
35. Greiner, M.T.; Helander, M.G.; Wang, Z.B.; Tang, W.M.; Qiu, J.; Lub, Z.H. A metallic molybdenum suboxide buffer layer for organic electronic devices. *Appl. Phys. Lett.* **2010**, *96*, 213302. [CrossRef]
36. Bouzidi, A.; Benramdane, N.; Tabet-Derraz, H.; Mathieu, C.; Khelifa, B.; Desfeux, R. Effect of substrate temperature on the structural and optical properties of MoO_3 thin films prepared by spray pyrolysis technique. *Mater. Sci. Eng. B* **2003**, *97*, 5–8. [CrossRef]
37. Sivakumar, R.; Gopalakrishnan, R.; Jayachandran, M.; Sanjeeviraja, C. Characterization on electron beam evaporated MoO_3 thin films by the influence of substrate temperature. *Curr. Appl. Phys.* **2007**, *7*, 51–59. [CrossRef]

38. Sivakumar, R.; Gopinath, C.S.; Jayachandran, M.; Sanjeeviraja, C. An electrochromic device (ECD) cell characterization on electron beam evaporated MoO_3 films by intercalating/deintercalating the H^+ ions. *Curr. Appl. Phys.* **2007**, *7*, 76–86. [CrossRef]
39. Macco, B.; Vos, M.; Thissen, N.F.W.; Bol, A.A.; Kessels, W.M.M. Low-temperature atomic layer deposition of MoO_x for silicon heterojunction solar cells. *Phys. Status Solidi: Rapid Res. Lett.* **2015**, *9*, 393–396.
40. Vos, M.F.J.; Macco, B.; Thissen, N.F.W.; Bol, A.A.; Kessels, W.M.M. Atomic layer deposition of molybdenum oxide from $(N^tBu)_2(NMe_2)_2Mo$ and O_2 plasma. *J. Vac. Sci. Technol. A* **2016**, *34*, 01A103. [CrossRef]
41. Haro-Poniatowski, E.; Jouanne, M.; Morhange, J.F.; Julien, C.; Diamant, R.; Fernandez-Guasti, M.; Fuentes, G.A.; Alonso, J.C. Micro-Raman characterization of WO_3 and MoO_3 thin films obtained by pulsed laser irradiation. *Appl. Surf. Sci.* **1998**, *127–129*, 674–678. [CrossRef]
42. Iriyama, Y.; Abe, T.; Inaba, M.; Ogumi, Z. Transmission electron microscopy (TEM) analysis of two-phase reaction in electrochemical lithium insertion within α-MoO_3. *Solid State Ionics* **2000**, *135*, 95–100. [CrossRef]
43. Hussain, O.M.; Srinivasa-Rao, K.; Madhuri, K.V.; Ramana, C.V.; Naidu, B.S.; Pai, S.; John, J.; Pinto, R. Growth and characteristics of reactive pulsed laser deposited molybdenum trioxide thin films. *Appl. Phys. A* **2002**, *75*, 417–422. [CrossRef]
44. Camacho-Lopez, M.A.; Escobar-Alarcon, L.; Haro-Poniatowski, E. Structural transformations in MoO_x thin films grown by pulsed laser deposition. *Appl. Phys. A* **2004**, *78*, 59–65. [CrossRef]
45. Bhosle, V.; Tiwari, A.; Narayan, J. Epitaxial growth and properties of MoO_x ($2 < x < 2.75$) films. *J. Appl. Phys.* **2005**, *97*, 083539.
46. Torres, J.; Alfonso, J.E.; Lopez-Carreno, L.D. XPS and X-ray diffraction characterization of MoO_3 thin films prepared by laser evaporation. *Phys. Status Solidi C* **2005**, *2*, 3726–3729. [CrossRef]
47. Puppala, H.K.; Pelton, A.T.; Mayanovic, R.A. A comparative characterization study of molybdenum oxide thin films grown using femtosecond and nanosecond pulsed laser deposition. *MRS Adv.* **2016**, *1*, 2585–2590. [CrossRef]
48. Liu, C.; Li, Z.; Zhang, Z. Growth of [010] oriented α-MoO_3 nanorods by pulsed electron beam deposition. *Appl. Phys. Lett.* **2011**, *99*, 223104. [CrossRef]
49. Robinson-Azariah, J.C.; Ponmudi-Selvan, T.; Rajasekar, M.S.; Sheebha, I.; Vidhya, B.; Rajesh, S. Pulsed laser deposited molybdenum oxides (MoO_3 and MoO_2) thin films for nanoelectronics device application. In Proceedings of the 4th Int. Conf. Devices, Circuits and Systems (ICDCS'18), Karunya Nagar, Coimbatore, India, 17–18 March 2018; pp. 42–47.
50. Al-Kuhaili, M.F.; Durrani, S.M.A.; Bakhtiari, I.A. Pulsed laser deposition of molybdenum oxide thin films. *Appl. Phys. A* **2010**, *98*, 609–615. [CrossRef]
51. Aoki, T.; Matsushita, T.; Mishiro, K.; Suzuki, A.; Okuda, M. Optical recording characteristics of molybdenum oxide films prepared by pulsed laser deposition method. *Thin Solid Films* **2008**, *517*, 1482–1486. [CrossRef]
52. Li, J.; Yin, J.; Li, X.; Zhou, J.; Guo, W. Chemical vapor deposition of ultra-thin molybdenum dioxide nanosheets. *Mater. Lett.* **2016**, *174*, 188–191. [CrossRef]
53. Vorobeva, N.S.; Lipatov, A.; Muratov, D.S.; Sinitskii, A. Chemical vapor deposition and characterization of two-dimensional molybdenum dioxide (MoO_2) nanoplatelets. *Nanotechnology* **2018**, *29*, 505707. [CrossRef]
54. Zhang, X.; You, F.; Zheng, Q.; Zhang, Z.; Cai, P.; Xue, X.; Xiong, J.; Zhang, J. Solution-processed MoO_x hole injection layer towards efficient organic light-emitting diode. *Org. Electron.* **2016**, *39*, 43–49. [CrossRef]
55. Santhosh, S.; Mathankumar, M.; Chandraekaran, S.S.; Nanda-Kumar, A.K.; Murugan, P.; Subramanian, B. Effect of ablation rate on the microstructure and electrochromic properties of pulsed-laser-deposited molybdenum oxide thin films. *Langmir* **2017**, *33*, 19–33. [CrossRef] [PubMed]
56. Julien, C.M.; Mauger, A. Pulsed laser deposited films for microbatteries. *Coatings* **2019**, *9*, 386. [CrossRef]
57. Al-Kuhaili, M.F.; Durrani, S.M.A.; Bakhtiari, I.A.; Al-Shukri, A.M. Optical constants and thermocoloration of pulsed laser deposited molybdenum oxide thin films. *Opt. Commun.* **2010**, *283*, 2857–2862. [CrossRef]
58. Kern, W. The evolution of silicon wafer cleaning technology. *J. Electrochem. Soc.* **1990**, *137*, 1887–1892. [CrossRef]
59. Xiao, X.; Song, H.; Lin, S.; Zhou, Y.; Zhan, X.; Hu, Z.; Zhang, Q.; Sun, J.; Yang, B.; Li, T.; et al. Scalable salt-templated synthesis of two-dimensional transition metal oxides. *Nat. Commun.* **2016**, *7*, 11296. [CrossRef]
60. Zhang, S.; Wang, G.; Jin, J.; Zhang, L.; Wen, Z.; Yang, J. Self-catalyzed decomposition of discharge products on the oxygen vacancy sites of MoO_3 nanosheets for low-overpotential Li-O_2 batteries. *Nano Energy* **2017**, *36*, 186–196. [CrossRef]

61. Guerfi, A.; Paynter, R.W.; Dao, L.H. Characterization and stability of electrochromic MoO_3 thin films prepared by electrodeposition. *J. Electrochem. Soc.* **1995**, *142*, 3457–3464. [CrossRef]
62. Navas, I.; Vinodkumar, R.; Lethy, K.J.; Detty, A.P.; Ganesan, V.; Sathe, V.; Mahadevan Pillai, V.P. Growth and characterization of molybdenum oxide nanorods by RF magnetron sputtering and subsequent annealing. *J. Phys. D Appl. Phys.* **2009**, *42*, 175305. [CrossRef]
63. Hari-Krishna, K.; Hussain, O.M.; Guillen, C. Photo- and electrochromic properties of activated reactive evaporated MoO_3 thin films grown on flexible substrates. *Res. Lett. Nanotechnol.* **2008**, *2008*, 217510.
64. Rahman, F.; Ahmed, T.; Walia, S.; Mayes, E.; Sriram, S.; Bhaskaran, M.; Balendhran, S. Reversible resistive switching behavior in CVD grown, large area MoO_x. *Nanoscale* **2018**, *10*, 19711–19719. [CrossRef] [PubMed]
65. Huang, Q.; Hu, S.; Zhuang, J.; Wang, X. MoO_{3-x}-based hybrids with tunable localized surface plasmon resonances: Chemical oxidation driving transformation from ultrathin nanosheets to nanotubes. *Chem. Eur. J.* **2012**, *18*, 15283–15287. [CrossRef] [PubMed]
66. Ding, D.; Huang, W.; Song, C.; Yan, M.; Guo, C.; Liu, S. Non-stoichiometric MoO_{3-x} quantum dots as a light-harvesting material for interfacial water evaporation. *Chem. Commun.* **2017**, *53*, 6744–6747. [CrossRef] [PubMed]
67. Eda, K. Raman spectra of hydrogen molybdenum bronze, $H_{0.30}MoO_3$. *J. Solid State Chem.* **1992**, *98*, 350–357. [CrossRef]
68. Liu, D.; Lei, W.; Chen, X.; Hao, J.; Jin, Y.; Cui, Q.; Zou, G. Pressure-induced structural transitions in $MoO_{3-x}H_2O$ (x = 1/2, 2) molybdenum trioxide hydrates: A Raman study. *J. Phys. Chem. B* **2009**, *113*, 16479–16482. [CrossRef]
69. Cotton, F.A.; Wing, R.M. properties of metal-to-oxygen multiple bonds, especially molybdenum-to-oxygen bonds. *Inorg. Chem.* **1965**, *4*, 867–873. [CrossRef]
70. Diskus, M.; Nilsen, O.; Fjellvag, H.; Diplas, S.; Beato, P.; Harvey, C.; Lantman, E.S.; Weckhuysen, B.M. Combination of characterization techniques for atomic layer deposition MoO_3 coatings: From the amorphous to the orthorhombic α-MoO_3 crystalline phase. *J. Vac. Sci. Technol. A* **2012**, *30*, 01A107. [CrossRef]
71. Ni, J.; Wang, G.; Yang, J.; Gao, D.; Chen, J.; Gao, L.; Li, Y. Carbon nanotube-wired and oxygen-deficient MoO_3 nanobelts with enhanced lithium-storage capability. *J. Power Sources* **2014**, *247*, 90–94. [CrossRef]
72. Chen, C.Z.; Li, Y.; Tang, X.D. Evidence of oxygen vacancy and possible intermediate gap state in layered α-MoO_3 single-crystal nanobelts. *Physica B* **2016**, *481*, 192–196. [CrossRef]
73. Lee, S.H.; Seong, M.J.; Tracy, C.E.; Mascarenhas, A.; Pitts, J.R.; Deb, S.K. Raman spectroscopic studies of electrochromic a-MoO_3 thin films. *Solid State Ionics* **2002**, *147*, 129–133. [CrossRef]
74. Cuando-Espitia, N.; Redenius, J.; Mensink, K.; Camacho-Lopez, M.; Camacho-Lopez, S.; Aguilar, G. Influence of oxygen pressure on the fs laser-induced oxidation of molybdenum thin films. *Opt. Mater. Express* **2018**, *8*, 581–596. [CrossRef]
75. Eda, K. Infrared spectra of hydrogen molybdenum bronze, $H_{0.34}MoO_3$. *J. Solid State Chem.* **1989**, *83*, 292–303. [CrossRef]
76. Mizuno, N.; Katamura, K.; Yoneda, Y.; Misono, M. Catalysis by heteropoly compounds: V. The reduction mechanism of $H_3PMo_{12}O_{40}$. *J. Catal.* **1983**, *83*, 384–392.
77. Dong, W.; Mansour, A.N.; Dunn, B. Structural and electrochemical properties of amorphous and crystalline molybdenum oxide aerogels. *Solid State Ionics* **2001**, *144*, 31–40. [CrossRef]
78. Sun, Y.; Takacs, C.J.; Cowan, S.R.; Seo, J.H.; Gong, X.; Roy, A.; Heeger, A.J. Efficient, air-stable bulk heterojunction polymer solar cells using MoO_x as the anode interfacial layer. *Adv. Mater.* **2011**, *23*, 2226–2230. [CrossRef]
79. Choi, J.-G.; Thompson, L.T. XPS study of as-prepared and reduced molybdenum oxides. *Appl. Surf. Sci.* **1996**, *93*, 143–149. [CrossRef]
80. Gacitua, M.; Boutaleb, Y.; Cattin, L.; Abe, S.Y.; Lare, Y.; Soto, G.; Louarn, G.; Morsli, M.; Rehamnia, R.; Del valle, A.; et al. Electrochemical preparation of MoO_3 buffer layer deposited onto the anode in organic solar cells. *Phys. Status Solidi A* **2010**, *207*, 1905–1911. [CrossRef]
81. Zeng, R.; Liu, H.; Shen, W. A facile and controllable electrochemically fabricated nonstoichiometric MoO_x film for novel opto-electronic devices. *J. Micromech. Microeng.* **2019**, *29*, 065012. [CrossRef]
82. Chang, L.L.Y.; Phillips, B. Phase relations in refractory metal–oxygen systems. *J. Am. Ceram. Soc.* **1969**, *52*, 527–533. [CrossRef]
83. Tong, J.; Wan, Y.; Cyi, J.; Lim, S.; Song, N.; Lennon, A. Solution-processed molybdenum oxide for hole-selective contacts on crystalline silicon solar cells. *Appl. Surf. Sci.* **2017**, *423*, 139–146. [CrossRef]

84. Novotny, P.; Lamb, H.H. Nanostructured MoO_x films deposited on c-plane sapphire. *J. Vac. Sci. Technol. A* **2019**, *37*, 051504. [CrossRef]
85. Fernandes-Cauduro, A.L.; Dos Reis, R.; Chen, G.; Schmid, A.K.; Méthivier, C.; Rubahn, H.G.; Bossard-Giannesini, L.; Cruguel, H.; Witkowski, N.; Madsen, M. Crystalline molybdenum oxide thin-films for application as interfacial layers in optoelectronic devices. *ACS Appl. Mater. Interfaces* **2017**, *9*, 7717–7724. [CrossRef] [PubMed]
86. Han, B.; Gao, M.; Wan, Y.; Li, Y.; Song, W.; Ma, Z. Effect of post-annealing on the properties of thermally evaporated molybdenum oxide films: Interdependence of work function and oxygen to molybdenum ratio. *Mater. Sci. Semicond. Proc.* **2018**, *75*, 166–172. [CrossRef]
87. Li, F.; Zhou, Y.; Liu, M.; Dong, G.; Liu, F.; Wang, W.; Yu, D. Molybdenum Oxide Hole Selective Transport Layer by Hot Wire Oxidation-Sublimation Deposition for Silicon Heterojunction Solar Cells. Available online: https://arxiv.org/ftp/arxiv/papers/1902/1902.09127.pdf (accessed on 25 February 2019).
88. Mehmood, H.; Bektas, G.; Yildiz, I.; Tauqeer, T.; Nasser, H.; Turan, R. Electrical, optical and surface characterization of reactive RF magnetron sputtered molybdenum oxide films for solar cell applications. *Mater. Sci. Semicond. Proc.* **2019**, *101*, 46–56. [CrossRef]
89. Li, Z.; Zhao, T.; Zhan, X.; Gao, D.; Xiao, Q.; Lei, G. High capacity three-dimensional ordered microporous $CoFe_2O_4$ as anode material for lithium ion batteries. *Electrochim. Acta* **2010**, *55*, 4594–4598. [CrossRef]
90. Yonekura, D.; Iwama, E.; Ota, N.; Muramatsu, M.; Saito, M.; Orikasa, Y.; Naoi, W.; Naoi, K. Progress of the conversion reaction of Mn_3O_4 particles as a function of the depth of discharge. *Phys. Chem. Chem. Phys.* **2014**, *16*, 6027–6032. [CrossRef]
91. Su, Q.; Wang, S.; Du, G.; Xu, B.; Ma, S.; Shang, L. Microstructure evolution and conversion mechanism of Mn_3O_4 under electrochemical cyclings. *Phys. Chem. C* **2018**, *122*, 2475–2480. [CrossRef]
92. Huang, S.Z.; Cai, Y.; Jin, J.; Liu, J.; Li, Y.; Yu, Y.; Wang, H.E.; Chen, L.H.; Su, B.L. Hierarchical mesoporous urchin-like Mn_3O_4/ carbon microspheres with highly enhanced lithium battery performance by in-situ carbonization of new lamellar manganese alkoxide (Mn-DEG). *Nano Energy* **2015**, *12*, 833–844. [CrossRef]
93. Dickens, P.G.; Reynolds, G.J. Transport and equilibrium properties of some oxide insertion compounds. *Solid State Ionics* **1981**, *5*, 331–334. [CrossRef]
94. Jung, Y.S.; Lee, S.K.; Ahn, D.J.; Dillon, A.C.; Lee, S.H. Electrochemical reactivity of ball-milled MoO_{3-y} as anode materials for lithium-ion batteries. *J. Power Sources* **2009**, *188*, 286–291. [CrossRef]
95. Bruce, P.G.; Scrosati, B.; Tarascon, J.M. Nanomaterials for rechargeable lithium batteries. *Angew. Chem. Int. Ed.* **2008**, *47*, 2930–2946. [CrossRef]
96. Zhang, X.; Jiang, W.J.; Mauger, A.; Gendron, F.; Julien, C.M.; Qilu, R. Minimization of the cation mixing in $Li_{1+x}(NMC)_{1-x}O_2$ as cathode material. *J. Power Sources* **2010**, *195*, 1292–1301. [CrossRef]
97. Hashem, A.M.; Abdel-Ghany, A.E.; Scheuermann, M.; Indris, S.; Ehrenberg, H.; Mauger, A.; Julien, C.M. Doped nanoscale NMC333 as cathode materials for Li-ion batteries. *Materials* **2019**, *12*, 2899. [CrossRef]
98. Brezesinski, T.; Wang, J.; Tolbert, S.H.; Dunn, B. Ordered mesoporous α-MoO_3 with iso-oriented nanocrystalline walls for thin-film pseudocapacitors. *Nat. Mater.* **2010**, *9*, 146–151. [CrossRef]
99. Hashem, A.M.; Groult, H.; Mauger, A.; Zaghib, K.; Julien, C.M. Electrochemical properties of α-MoO_3 as cathode materials for Li batteries. *J. Power Sources* **2012**, *219*, 126–132. [CrossRef]
100. Weppner, W.; Huggins, R.A. Determination of the kinetic parameters of mixed-conducting electrodes and application to the system Li_3Sb. *J. Electrochem. Soc.* **1977**, *124*, 1569–1578. [CrossRef]
101. Wen, C.J.; Boukamp, B.A.; Huggins, R.A.; Weppner, W. Thermodynamic and mass transport properties of LiAl. *J. Electrochem. Soc.* **1979**, *126*, 2258–2266. [CrossRef]
102. Jang, Y.I.; Neudecker, B.J.; Dudney, N.J. Lithium diffusion in Li_xCoO_2 (0.45 <x <0.7 intercalation cathodes. *Electrochem. Solid-State Lett.* **2001**, *4*, A74–A77.
103. Tang, S.B.; Lai, M.O.; Lu, L. Li-ion diffusion in highly (003) oriented $LiCoO_2$ thin film cathode prepared by pulsed laser deposition. *J. Alloys Compd.* **2008**, *449*, 300–303. [CrossRef]
104. Honders, A.; der Kinderen, J.M.; van Heeren, A.H.; de Wit, J.H.W.; Broers, G.H.J. Bounded diffusion in solid solution electrode powder compacts. Part II. The simultaneous measurement of the chemical diffusion coefficient and the thermodynamic factor in Li_xTiS_2 and Li_xCoO_2. *Solid State Ionics* **1985**, *15*, 265–276. [CrossRef]
105. Levi, M.D.; Aurbach, D. Frumkin intercalation isotherm—A tool for the description of lithium insertion into host materials: Areview. *Electrochim. Acta* **1999**, *45*, 167–185. [CrossRef]

106. Montella, C. Discussion of the potential step method for the determination of the diffusion coefficients of guest species in host materials Part I. Influence of charge transfer kinetics and ohmic potential drop. *J. Electroanal. Chem.* **2002**, *518*, 61–83. [CrossRef]
107. Carcia, P.F.; McCarron, E.M. Synthesis and properties of thin films polymorphs of molybdenum trioxide. *Thin Solid Films* **1987**, *155*, 53–63. [CrossRef]
108. Altman, E.I.; Droubay, T.; Chambers, S.A. Growth of MoO_3 films by oxygen plasma assisted molecular beam epitaxy. *Thin Solid Films* **2002**, *414*, 205–215. [CrossRef]
109. Siokou, A.; Leftheriotis, G.; Papaefthimiou, S.; Yianoulis, P. Effect of the tungsten and molybdenum oxidation states on the thermal coloration of amorphous WO_3 and MoO_3 films. *Surf. Sci.* **2001**, *482–485*, 294–299. [CrossRef]
110. Ressler, T.; Jentoft, R.E.; Wienold, J.; Günter, M.M.; Timpe, O. In situ XAS and XRD studies on the formation of Mo suboxides during reduction of MoO_3. *J. Phys. Chem. B* **2000**, *104*, 6360–6370. [CrossRef]
111. Anbananthan, N. Studies on oxygen deficient molybdenum oxide electrodes. *Bull. Electrochem.* **2003**, *19*, 79–84.
112. Hashem, A.M.A.; Abbas, S.; Abdel-Ghany, A.; Julien, C.M. Blend formed by oxygen deficient $MoO_{3-\delta}$ oxides as lithium-insertion compounds. *J. Alloys Compd.* **2016**, *686*, 744–752. [CrossRef]
113. Alfonso, J.E.; Moreno, L.C. Preparation and chemical characterization of neodymium-doped molybdenum oxide films grown using spray pyrolysis. *Rev. Mex. Fis.* **2014**, *60*, 114–118.
114. Yeh, H.L.; Tai, S.H.; Hsieh, C.M.; Chang, B.K. First-principles study of lithium intercalation and diffusion in oxygen-defective titanium dioxide. *J. Phys. Chem. C* **2018**, *122*, 19447–19454. [CrossRef]
115. Luo, H.C.; Martin, M. Investigation of the phase diagram and the defect structure of nonstoichiometric $Li_{1+x}Mn_{2-x}O_{4-\delta}$ ($0 \leq x \leq 0.33$) spinel. *Electrochem. Soc. Proc.* **2003**, *2003*, 281–288.
116. Dong, W.; Xu, J.; Wang, C.; Lu, Y.; Liu, X.; Wang, X.; Yuan, X.; Wang, Z.; Lin, T.; Sui, M.; et al. A Robust and conductive black tin oxide nanostructure makes efficient lithium-ion batteries possible. *Adv. Mater.* **2017**, *29*, 1700136. [CrossRef] [PubMed]
117. Zheng, Y.; Zhou, T.; Zhao, X.; Pang, W.K.; Gao, H.; Li, S.; Zhou, Z.; Liu, H.; Guo, Z. Atomic interface engineering and electric-field effect in ultrathin Bi_2MoO_6 nanosheets for superior lithium ion storage. *Adv. Mater.* **2017**, *29*, 1700396. [CrossRef] [PubMed]
118. Zhu, J.; Chen, J.; Xu, H.; Sun, S.; Xu, Y.; Zhou, M.; Gao, X.; Sun, Z. Plasma-introduced oxygen defects confined in $Li_4Ti_5O_{12}$ nanosheets for boosting lithium-ion diffusion. *ACS Appl. Mater. Interfaces* **2019**, *11*, 17384–17392. [CrossRef]
119. Zhang, Y.; Tao, L.; Xie, C.; Wang, D.; Zou, Y.; Chen, R.; Wang, Y.; Jia, C.; Wang, S. Defect engineering on electrode materials for rechargeable batteries. *Adv. Mater.* **2020**, *32*, 1905923. [CrossRef]
120. Xiong, T.; Yu, Z.G.; Wu, H.; Du, Y.; Xie, Q.; Chen, J.; Zhang, Y.-W.; Pennycook, S.J.; Lee, W.S.; Xue, J. Defect engineering of oxygen-deficient manganese oxide to achieve high-performing aqueous zinc ion battery. *Adv. Energy Mater.* **2019**, *9*, 1803815. [CrossRef]
121. Qiao, X.; Chen, J.; Li, X.; Dongge, M. Observation of hole hopping via dopant in MoO_x-doped organic semiconductors: Mechanism analysis and application for high performance organic light-emitting devices. *J. Appl. Phys.* **2010**, *107*, 104505. [CrossRef]
122. Guo, Y.; Robertson, J. Origin of the high work function and high conductivity of MoO_3. *Appl. Phys. Lett.* **2014**, *105*, 222110. [CrossRef]
123. Meduri, P.; Clark, E.; Kim, J.H.; Dayalan, E.; Sumanasekera, G.U.; Sunkara, M.K. MoO_{3-x} nanowire arrays as stable and high-capacity anodes for lithium ion batteries. *Nano Lett.* **2012**, *12*, 1784–1788. [CrossRef]
124. Zhao, G.; Zhang, N.; Sun, K. Electrochemical preparation of porous MoO_3 film with a high rate performance as anode for lithium ion batteries. *J. Mater. Chem. A* **2013**, *1*, 221–224. [CrossRef]
125. Chen, W.; Zhang, H.; Wang, Y.; Ma, Z.; Li, Z. In-situ microstructural investigations by electron-beam irradiation induced crystallization of amorphous MoO_x thin films with high performance for Li-ion storage. *Electrochim. Acta* **2014**, *144*, 369–375. [CrossRef]
126. Wang, Y.; Zhu, Y.; Xing, Z.; Qian, Y. Hydrothermal synthesis of α-MoO_3 and the influence of later heat treatment on its electrochemical properties. *Int. J. Electrochem. Sci.* **2013**, *8*, 9851–9857.
127. Ahmed, B.; Shahid, M.; Nagaraju, D.H.; Anjum, D.H.; Hedhili, M.N.; Alshareef, H.N. Surface passivation of MoO_3 nanorods by atomic layer deposition towards high rate durable Li ion battery anodes. *ACS Appl. Mater. Interfaces* **2015**, *7*, 13154–13163. [CrossRef] [PubMed]

128. Wu, D.; Shen, R.; Yang, R.; Ji, W.; Jiang, M.; Ding, W.; Peng, L. Mixed molybdenum oxides with superior performances as an advanced anode material for lithium-ion batteries. *Sci. Rep.* **2017**, *7*, 44697. [CrossRef]
129. Lee, S.H.; Deshpande, R.; Benhammou, D.; Parilla, P.A.; Mahan, A.H.; Dillon, A.C. Metal oxide nanoparticles for advanced energy applications. *Thin Solid Films* **2009**, *517*, 3591–3595. [CrossRef]
130. Xue, X.-Y.; Chen, Z.-H.; Xing, L.-L.; Yuan, S.; Chen, Y.-J. SnO_2/α-MoO_3 core-shell nanobelts and their extraordinarily high reversible capacity as lithium-ion battery anodes. *Chem. Commun.* **2011**, *47*, 5205–5207. [CrossRef]
131. Riley, L.A.; Lee, S.H.; Gedvilias, L.; Dillon, A.C. Optimization of MoO_3 nanoparticles as negative-electrode material in high-energy lithium ion batteries. *J. Power Sources* **2010**, *195*, 588–592. [CrossRef]
132. Lee, S.H.; Kim, Y.H.; Deshpande, R.; Parilla, P.A.; Whitney, E.; Gillaspie, D.T.; Jones, K.M.; Mahan, A.H.; Zhang, S.B.; Dillon, A.C. Reversible lithium-ion insertion in molybdenum oxide nanoparticles. *Adv. Mater.* **2008**, *20*, 3627–3632. [CrossRef]
133. Ette, P.M.; Ramesha, P.G.K. Self-assembled lamellar alpha-molybdenum trioxide as high performing anode material for lithium-ion batteries. *J. Power Sources* **2015**, *278*, 630–638. [CrossRef]
134. Xu, Y.; Zhou, M.; Wang, X.; Wang, C.; Liang, L.; Grote, F.; Wu, M.; Mi, Y.; Lei, Y. Enhancement of sodium ion battery performance enabled by oxygen vacancies. *Angew. Chem. Int. Ed.* **2015**, *54*, 8768–8771. [CrossRef]
135. Icovi, M.; Panero, S.; D'Agate, A.; Pistoia, G.; Temperoni, C. Non-Stoichiometric molybdenum oxides as cathodes for lithium cells. Part II. Secondary batteries. *J. Electroanal. Chem.* **1979**, *102*, 343–349. [CrossRef]
136. Feng, C.; Gao, H.; Zhang, C.; Guo, Z.; Liu, H. Synthesis and electrochemical properties of MoO_3/C nanocomposite. *Electrochim. Acta* **2013**, *93*, 101–106. [CrossRef]
137. Hassan, M.F.; Guo, Z.P.; Chen, Z.; Liu, H.K. Carbon-coated MoO_3 nanobelts as anode materials for lithium-ion batteries. *J. Power Sources* **2010**, *195*, 2372–2376. [CrossRef]
138. Liu, C.-L.; Wang, Y.; Zhang, C.; Li, X.-S.; Dong, W.-S. In situ synthesis of a-MoO_3/graphene composites as anode materials for lithium ion battery. *Mater. Chem. Phys.* **2014**, *143*, 1111–1118. [CrossRef]
139. Ma, F.; Yuan, A.; Xu, J.; Hu, P. Porous α-MoO_3/MWCNT nanocomposite synthesized via a surfactant-assisted solvothermal route as a lithium-ion-battery high-capacity anode material with excellent rate capability and cyclability. *ACS Appl. Mater. Interfaces* **2015**, *7*, 15531–15541. [CrossRef] [PubMed]
140. Julien, C.; Khelfa, A.; Guesdon, J.P.; Gorenstein, A. Lithium intercalation in MoO_3: A comparison between crystalline and disordered phases. *Appl. Phys. A* **1994**, *59*, 173–178. [CrossRef]
141. Julien, C.; Nazri, G.A.; Guesdon, J.P.; Gorenstein, A.; Khelfa, A.; Hussain, O.M. Influence of the growth conditions on electrochemical features of MoO_3 film-cathodes in lithium microbatteries. *Solid State Ionics* **1994**, *73*, 319–326. [CrossRef]
142. Halalay, I.C.; Nazri, G.-A.; Cheng, Y.-T.; Eesley, G.L.; Meyer, M.S. Optical measurement of lithium diffusivity in cathode materials: Amorphous MoO_3 films. *J. Power Sources* **1995**, *54*, 218–220. [CrossRef]
143. Zhao, X.; Jia, W.; Wu, X.; Lv, Y.; Qiu, J.; Guo, J.; Wang, X.; Jia, D.; Yan, J.; Wu, D. Ultrafine MoO_3 anchored in coal-based carbon nanofibers as anode for advanced lithium-ion batteries. *Carbon* **2020**, *156*, 445–452. [CrossRef]
144. Ding, J.; Abbas, S.A.; Hanmandlu, C.; Lin, L.; Lai, C.S.; Wang, P.C.; Li, L.J.; Chu, C.W.; Chang, C.C. Facile synthesis of carbon/MoO_3 nanocomposites as stable battery anodes. *J. Power Sources* **2017**, *348*, 270–280. [CrossRef]
145. Xia, Q.; Zhao, H.; Du, Z.; Zeng, Z.; Gao, C.; Zhang, Z.; Du, X.; Kulka, A.; Swierczek, K. Facile synthesis of MoO_3/carbon nanobelts as high-performance anode material for lithium ion batteries. *Electrochim. Acta* **2015**, *180*, 947–956. [CrossRef]
146. Yu, Z.; Jiang, H.; Gu, D.; Li, J.; Wang, L.; Shen, L. A new way to prepare MoO_3/C as anode of lithium ion battery for enhancing the electrochemical performance at room temperature. *J. Electrochem. Sci. Technol.* **2016**, *7*, 170–178. [CrossRef]
147. Sun, Z.; Yang, C.; Liu, G.; Lu, H.; Zhang, R.; Wang, L.; Wang, H. Largely enhanced electrochemical performance in MoO_{3-x} nanobelts formed by a "sauna reaction": Importance of oxygen vacancies. *Electrochim. Acta* **2017**, *239*, 16–24. [CrossRef]
148. Tysyachny, V.P.; Shembel, E.M.; Apostolova, R.D.; Nagirny, V.M.; Kylyvnyk, K.E.; Eskova, N.I. Studies of the lithium ion transport properties in electrolytic molybdenum oxides. *Solid State Ionics* **2004**, *169*, 135–137. [CrossRef]

149. Xie, J.; Kohno, K.; Matsumura, T.; Imanishi, N.; Hirano, A.; Takeda, Y.; Yamamoto, O. Li-ion diffusion kinetics in $LiMn_2O_4$ thin films prepared by pulsed laser deposition. *Electrochim. Acta* **2008**, *54*, 376–381. [CrossRef]
150. Julien, C.; Haro-Poniatowski, E.; Camacho-Lopez, M.A.; Escobar-Alarcon, L.; Jimenez-Jarquin, J. Growth of $LiMn_2O_4$ thin films by pulsed-laser deposition and their electrochemical properties in lithium microbatteries. *Mater. Sci. Eng. B* **2000**, *72*, 36–46. [CrossRef]
151. Xie, J.; Imanishi, N.; Zhang, T.; Hirano, A.; Takeda, Y.; Yamamoto, O. Li-ion diffusion kinetics in $LiFePO_4$ thin films prepared by radio frequency magnetron sputtering. *Electrochim. Acta* **2009**, *54*, 4631–4637. [CrossRef]
152. Ho, C.; Raistrick, I.D.; Huggins, R.A. Application of A-C techniques to the study of lithium diffusion in tungsten trioxide thin films. *J. Electrochem. Soc.* **1980**, *127*, 343–350. [CrossRef]
153. Ding, N.; Xu, J.; Yao, Y.X.; Wegner, G.; Fang, X.; Chen, C.H.; Lieberwirth, I. Determination of the diffusion coefficient of lithium ions in nano-Si. *Solid State Ionics* **2009**, *180*, 222–225. [CrossRef]
154. Maier, J. Diffusion in materials with ionic and electronic disorder. *Mater. Res. Soc. Symp. Proc.* **1991**, *210*, 499. [CrossRef]
155. Wu, C.; Xie, H.; Li, D.; Liu, D.; Ding, S.; Tao, S.; Chen, H.; Liu, Q.; Chen, S.; Chu, W.; et al. Atomically intercalating tin ions into the interlayer of molybdenum oxide nanobelt toward long-cycling lithium battery. *J. Phys. Chem. Lett.* **2018**, *9*, 817–824. [CrossRef] [PubMed]
156. Julien, C.; Yebka, B.; Ziolkiewicz, S.; Doi, A. Lithium insertion in molybdenum and vanadium oxide films. *Electrochem. Soc. Proc.* **1997**, *97-24*, 862–873.
157. Lee, Y.-S.; Ruy, K.-S. Study of the lithium diffusion properties and high rate performance of $TiNb_6O_{17}$ as an anode in lithium secondary battery. *Sci. Rep.* **2017**, *7*, 16617. [CrossRef] [PubMed]
158. Kulova, T.L.; Skundin, A.M.; Pleskov, Y.V.; Terukov, E.I.; Kon'kov, O.I. Lithium intercalation in thin amorphous-silicon films. *Russian J. Electrochem.* **2006**, *42*, 363–369. [CrossRef]
159. Sivonxay, E.; Aykol, M.; Persson, K.A. The lithiation process and Li diffusion in amorphous SiO_2 and Si from first-principles. *Electrochim. Acta* **2020**, *331*, 135344. [CrossRef]
160. Ostadhossein, A.; Kim, S.-Y.; Cubuk, E.D.; Qi, Y.; van Duin, A.C.T. Atomic insight into the lithium storage and diffusion mechanism of SiO_2/Al_2O_3 electrodes of lithium ion batteries: ReaxFF reactive force field modeling. *J. Phys. Chem. A* **2016**, *120*, 2114–2127. [CrossRef]
161. Kulova, T.L.; Skundin, A.M.; Nizhnikovskii, E.A.; Fesenko, A.V. Temperature effect on the lithium diffusion rate in graphite. *Russ. J. Electrochem.* **2006**, *42*, 259–262. [CrossRef]
162. Gong, J.; Wu, H. Electrochemical intercalation of lithium species into disordered carbon prepared by the heat-treatment of poly (p-phenylene) at 650 °C for anode in lithium-ion battery. *Electrochim. Acta* **2000**, *45*, 1753–1762. [CrossRef]
163. Yang, H.; Bang, H.J.; Prakash, J. Evaluation of electrochemical interface area and lithium diffusion coefficient for a composite graphite anode. *J. Electrochem. Soc.* **2004**, *151*, A1247–A1250. [CrossRef]
164. Panchmatia, P.M.; Armstrong, A.R.; Bruce, P.G.; Islam, M.S. Lithium-ion diffusion mechanisms in the battery anode material $Li_{1+x}V_{1-x}O_2$. *Phys. Chem. Chem. Phys.* **2014**, *16*, 21114–21118. [CrossRef]